# Understanding the Reaction of Nuclear Graphite with Molecular Oxygen: Kinetics, Transport, and Structural Evolution

Joshua J. Kane,[a] Cristian I. Contescu,[b] Rebecca E. Smith,[a] Gerhard Strydom,[c] William E. Windes[a]

[a]Materials Science & Engineering Department, Energy & Environmental Science and Technology, Idaho National Laboratory, Idaho Falls, ID 83415, USA

[b]Materials Science and Technology Division, Oak Ridge National Laboratory, Oak Ridge, Tennessee, USA

[c]Reactor Physics Design & Analysis, Nuclear Science and Technology, Idaho National Laboratory, Idaho Falls, ID 83415

*Corresponding author. Tel +1 208 526 5488; E-mail address: Joshua.kane@inl.gov

Keywords: Graphite, oxidation, universal model, microstructure, kinetics, mass transport, structural evolution

## Abstract

A thorough understanding of oxidation is important when considering the health and integrity of graphite components in graphite reactors. For the next generation of graphite reactors, HTGRs specifically, an unlikely air ingress has been deemed significant enough to have made its way into the licensing applications of many international licensing bodies. While a substantial body of literature exists on nuclear graphite oxidation in the presence of molecular oxygen and significant efforts have been made to characterize oxidation kinetics of various grades, the value of existing information is somewhat limited. Often, multiple competing processes, including reaction kinetics, mass transfer, and microstructural evolution, are lumped together into a single rate expression that limits the ability to translate this information to different conditions. This article reviews the reaction of graphite with molecular oxygen in terms of the reaction kinetics, gas transport, and microstructural evolution of graphite. It also presents the foundations of a model for the graphite-molecular oxygen reaction system that is kinetically independent of graphite grade, and is capable of describing both the bulk and local oxidation rates under a wide range of conditions applicable to air-ingress.

# Table of Contents

# Front Matter

## Terminology

Elementary Reaction Rate - The reaction rate of an elementary reaction. An elementary reaction can loosely be defined as one that involves a single step. Most gas-solid reactions, including the reaction of graphite with oxygen do not occur in a single step. Instead the reaction occurs via multiple elementary reactions in series and parallel. These elementary reactions working in concert form the reaction mechanism.

Effective Reaction Rate - An effective reaction rate is used here to describe the net kinetic rate of the graphite-oxygen reaction mechanism. The effective rate may be dictated by one elementary reaction or many elementary reactions simultaneously. An effective reaction rate can only be obtained from experimental data under conditions where the chemical reaction is the rate limiting process. This is represented by Regime 1 of Fig. 2 and for those familiar with the Thiele modulus, when $\phi_n \rightarrow 0$.

Observed Reaction Rate - Observed reaction rate is used here in a broad sense to represent typical rate data for the graphite-oxygen reaction system collected from experimental specimens in the literature. Commonly, this is collected by measuring mass loss as a function of time. Observed reaction rates are likely influenced, at least to some degree, by mass and heat transport. Another way of saying this is mass or heat transfer effects produce local gas composition and temperature variations within a graphite sample. Since the effective reaction rate is dependent upon these variables, the effective reaction rate will vary locally throughout the sample and often the observed rate will be different from the effective rate at the nominal experimental conditions.

Although under a very narrow and nearly ideal set of conditions, the observed reaction rate approaches the effective reaction rate, the following text assumes that mass and/or heat transfer play an appreciable role in the observed rate, unless explicitly stated otherwise. Observed rates may be purely described as a mass loss rate, but are commonly normalized to an extrinsic factor such as initial mass, instantaneous mass, volume, or geometric surface area. In general, the term observed reaction rate may be used interchangeably to some degree with terms such as apparent and bulk reaction rates. In the text below, these synonyms are avoided.

Intrinsic Reaction Rate - Gas-solid reactions inevitably involve surfaces and a quick survey of literature will show that different nuclear graphite grades often have significantly different oxidation rates under identical conditions. Generally speaking, it is the microstructural differences and ultimately the pore surface and its morphology that drive the observed differences in rate. The intrinsic reaction rate is considered below to be an inherent property of graphite dependent only upon the temperature and concentration(s) of reactive species. It is therefore independent of the quantity of graphite (size of specimen) or its microstructure (grade and time dependency). For graphite, the intrinsic reaction rate should be normalized to reactive

surface area. In the text below, discussion of intrinsic rates will mainly refer to an effective reaction rate that is normalized to reactive surface area.

**Nomenclature**

All symbols are listed in order of appearance.

| Symbol | Description | Units/Value | Equation(s) |
|---|---|---|---|
| $\boldsymbol{\phi_n}$ | Thiele modulus: ${\phi_n}^2$ relates the ratio of surface reaction rate to an effective rate of diffusion through a porous material. | *Unitless* | NA |
| $\boldsymbol{k_0}$ | A rate constant used for a semi-empirical fit of experimental data to a rate law. | *Varies* | 1,2 |
| $\boldsymbol{E_A}$ | Activation energy | $\frac{kJ}{mol}$ | 1,2 |
| $\boldsymbol{R}$ | Universal gas constant | $8.3145\ \frac{J}{mol\,K}$ | 1,2 |
| $\boldsymbol{T}$ | Temperature | $K$ or $°C$ | 1,2,12,13, 25,30 |
| $\boldsymbol{n}$ | Reaction order | *Unitless* | 1,2 |
| $\boldsymbol{P_{O_2}}$ | Partial pressure of molecular oxygen gas | $Varies$ | 1 |
| $[\boldsymbol{O_2}]$ | Concentration of molecular oxygen gas | $\frac{mol}{m^3}$ | 2,11-13, 19,21-23,25 |
| $\boldsymbol{x}$ | Stoichiometric coefficient of $CO(g)$. Purposely expressed as seen in Eq. (5) to represent the fraction of $CO(g)$ gaseous product | *Unitless* | 3,21-23,25 |
| $\boldsymbol{C_e}$ | Carbon edge atom at a {100} and {110} surface | *NA* | 4,5,7,8 |
| $\boldsymbol{C_e(O_2)}$ | Surface dioxranyl reactive intermediate | *NA* | 4,5,7 |
| $\boldsymbol{C_e(O)}$ | Surface semiquinone reactive intermediate | *NA* | 4,5,7 |
| $\boldsymbol{C_b}$ | Carbon atom within basal plane, (001) surface | *NA* | 5,6,8 |
| $\boldsymbol{C_b(O)}$ | Stable/mobile surface intermediate, epoxy bridge | *NA* | 5-7 |
| $\boldsymbol{k_{A1}}$ | Reaction rate constant for Eq. (4a) | Kane et al [29] | 4a,11,13 |
| $\boldsymbol{k_{A2}}$ | Reaction rate constant for Eq. (4b) | Kane et al [29] | 4b,11,13 |
| $\boldsymbol{k_S}$ $\boldsymbol{k_S^*}$ | Reaction rate constant for Eq. (5) | Kane et al [29] | 5,11,13 |
| $\boldsymbol{k_{Hop}}$ | Reaction rate constant for Eq. (6) | Kane et al [29] | 6 |
| $\boldsymbol{k_{D1}}$ $\boldsymbol{k_{D1}^*}$ | Reaction rate constant for Eq. (7a) | Kane et al [29] | 7a,10,11,13 |
| $\boldsymbol{k_{D2}}$ $\boldsymbol{k_{D2}^*}$ | Reaction rate constant for Eq. (7b) | Kane et al [29] | 7b,10,11,13 |
| $\boldsymbol{k_{D3}}$ $\boldsymbol{k_{D3}^*}$ | Reaction rate constant for Eq. (7c) | Kane et al [29] | 7c,10,11,13 |
| $\boldsymbol{k_{NSD}}$ | Reaction rate constant for Eq. (8) | Kane et al [29] | 8 |
| $\boldsymbol{\theta}$ | Surface coverage as defined in Eq. (9) | *Unitless* | 9 |
| $\boldsymbol{N_C}$ | Carbon molar flux towards the graphite surface | $\frac{mol}{m^2 s}$ | 10-12 |
| $[\boldsymbol{C_e(O_2)}]$ | Surface density of dioxyranyl reactive intermediate | $\frac{mol}{m^2}$ | 10 |

| Symbol | Description | Units/Value | Equation(s) |
|---|---|---|---|
| $[C_e(O)]$ | Surface density of semiquinone reactive intermediate | $\frac{mol}{m^2}$ | 10 |
| $\Gamma_e$ | Surface density of ASA | $\frac{mol}{m^2}$ | 11,13 |
| $k''_{eff}$ | Effective reaction rate constant for graphite-oxygen reaction normalized to ASA | $\frac{m}{s}$ | 12,13,,19,21 23,25 |
| $N_A$,$N_B$, $N_i$ | Gaseous flux of arbitrary gaseous species A or B or specific gaseous component i | $\frac{mol}{m^2 s}$ | 14-16, 20-24, |
| $C_T$ | Total gas phase concentration | $\frac{mol}{m^3}$ | 14,15,20 |
| $D_{AB}$ | Binary gaseous diffusion coefficient for arbitrary species A and B | $\frac{m^2}{s}$ | 14,15,31 |
| $y_A$ | Mole fraction of arbitrary gaseous species A | *Unitless* | 14,15 |
| $\rho$ | Molar density of graphite. A subscript of 0 indicates the initial density. | $\frac{mol}{m^3}$ | 19,26-28 |
| $t$ | time | s | 19,21-28 |
| $\varepsilon$ | Porosity by volumetric fraction | *Unitless* | 21-24,32,34 |
| $[CO]$ | Concentration of carbon monoxide gas | $\frac{mol}{m^3}$ | 19 |
| $[CO_2]$ | Concentration of carbon dioxide gas | $\frac{mol}{m^3}$ | 19 |
| $S_A$ | ASA of graphite of interest per unit volume | $\frac{1}{m}$ | 19,20-23,25 |
| $D_{eff_{iM}}$ | Effective diffusivity of species i through mixture M within a porous graphite material | $\frac{m^2}{s}$ | 20,29,31 |
| $y_i$ | Mole fraction of species i in gas phase | *Unitless* | 20,29 |
| $c_p$ | Molar specific heat of graphite | $\frac{J}{mol\ K}$ | 25 |
| $k_T$ | Observed thermal conductivity of nuclear graphite | $\frac{W}{m\ K}$ | 25,30,33 |
| $\Delta H_{rxn}$ | Enthalpy of Reaction for Eq. (3) | $\frac{J}{mol}$ | 25 |
| $r_{Obs}$ | Observed reaction rate | $\frac{mol}{s}$ | 26 |
| $V$ | Volume. Used only in a differential form. | *Varies* | 26-28 |
| $\alpha$ | Fractional conversion of graphite to gaseous product. *Example:* $\alpha = 1 - \frac{\Delta m}{m_0}$ | *Unitless* | 27,28 |
| $z$ | Length along an arbitrary coordinate direction of interest to oxidizing graphite sample | *Varies* | 28 |
| $k_{x,loc}$ | Local mass transfer coefficient along exterior graphite-gas interface | $\frac{mol}{m^2 s}$ | 29 |
| $\theta_y$ | Correction for mass transfer coefficient to account for a net flow of mass across the gas- | *Unitless* | 29 |

| Symbol | Description | Units/Value | Equation(s) |
|---|---|---|---|
| | solid interface | | |
| $h_{x,loc}$ | Local heat transfer coefficient along exterior of graphite-gas interface | $\frac{W}{m^2 K}$ | 30 |
| $\theta_T$ | Correction for heat transfer coefficient to account for a net flow of mass across the gas-solid interface | *Unitless* | 30 |
| $f_p$ | Porous structural factor defined in Eq. (31) | *Unitless* | 31,32 |
| $\sigma$ | A constriction factor accounting for decreases in the mass or heat transfer rate due to periodic expansions and contractions of a pores or solid cross-sectional area, respectively. A subscript G indicates the solid material rather than the pore structure. | *Unitless* | 32 |
| $\tau$ | Geodesic tortuosity factor accounting for the increase in distance traveled through a material relative to the sample coordinate system. A subscript G indicates the solid material rather than the pore structure. | *Unitless* | 32 |
| $k_G$ | Graphite thermal conductivity. The observed effect of the pore structure is removed. | $\frac{W}{m\,K}$ | 33 |
| $f_G$ | A structural factor for graphite defined in Eq. (33) | | 33,34 |

## 1. Prologue

This review article is intended to serve three intertwined purposes. The first is to thoroughly cover the major as well as more subtle features of the graphite-oxygen reaction system that influence the observed rate of graphite oxidation. To the best of the authors' knowledge no such article has been published on the subject for nuclear graphite in quite some time. Secondly, utilizing this understanding, we wish to make note of the highly conservative nature of classic oxidation models as well as their inability to account for several well-known (and well documented in literature) observations. While the conservative application of the classic oxidation model has been demonstrated adequate for the safety of historic graphite reactor designs, the more extreme materials environments inherent to more recently developed high temperature gas-cooled reactor designs may require (or at least benefit significantly from) a more detailed understanding and approach to the graphite-molecular oxygen reaction system. Finally, using only existing concepts and methodologies from the vast carbon-science literature, we wish to lay a foundation for an improved oxidation model. Classically, as a nuclear graphite community, we focus on fitting mass loss data for various grades of nuclear graphite in order to determine the oxidation kinetics of a grade of graphite. While this may work to some degree, this methodology convolutes the reaction kinetics, mass transport, and dynamic microstructural evolution together. Here we encourage the use of an intrinsic chemical reaction rate for the graphite-oxygen reaction. Such an approach should be independent of graphite grade and

therefore allow the decoupling of a graphite's microstructure from the observed reaction kinetics and gas transport. Ultimately there are three key advantages to this proposed intrinsic approach: (1) any nuclear grade graphite can be modeled using the same reaction kinetics and its particular observed rate can be determined using quantifiable characterization of the microstructure. (2) The oxidation rate is predicted locally throughout the graphite volume of interest and therefore the local microstructural damage may also be predicted. (3) This approach lends itself to better forecasting of oxidation rates after a graphite has been in an irradiation environment for some time and its microstructure has evolved.

# 2. Introduction

The reactions of carbon with oxygen, in one form or another, are quite possibly the most studied set of chemical reactions known to mankind. This is largely due to the consumption of carbonaceous materials for electrical power production. According to the World Coal Association as of 2014, coal is the second largest energy source, accounting for 30.1% of global primary energy consumption. Roughly 41% of the world's electricity is supplied by coal-fired power plants and coal is used in the production of over 70% of the word's steel supply. Even with a below average global primary energy consumption growth of 1.0% in 2015 (10 year average growth of 1.9%) [1] there is an increased interest in alternative and low-carbon-emitting energy technologies to mitigate the effects of increasing carbon dioxide levels.

## 2.1. Nuclear Application of Graphite

Nuclear power is one possible low-carbon emission technology with a substantial and consistent power output. Graphite reactors have historically represented an alternative route to the dominant role of water-moderated LWRs in the generation of civilian nuclear power. These have included the Magnox/UNGG (UK), the RBMK (Russia), the General Atomics Fort St Vrain HTGR (USA) and the UK Advanced Gas-Cooled designs, some of which are still in operation. The next generation of graphite reactors will likely be of the smaller modular High Temperature Gas-cooled Reactor (HTGR) or Molten Salt Reactor design [2].

HTGRs are inherently safe, helium-cooled, graphite-moderated reactors that have been tested and operated since the 1960s. New HTGRs under consideration include both pebble and prismatic fuel form designs. The nuclear heat supply system for recent modular HTGR designs under consideration in the United States of America are rated from 200 MWt to 625 MWt with reactor outlet temperatures from 700°C to 850°C [3]. This allows energy to be transported through steam and/or another high-temperature fluid medium for the generation of electrical power at high levels of efficiency. Additionally, the modular HTGR design's high outlet temperatures provide a flexible energy source for a wide range of energy intensive industrial processes [2].

Graphite is a crucial materials component of the HTGR. It serves as the neutron moderator medium (allowing the thermalization of fast neutrons), a structural component, a medium for the

efficient storage and transport of heat away from the fuel and fuel matrix; and in the extremely unlikely event of a significant accident with air-ingress, it serves as a protective enclosure for fuel in both pebble and prismatic HTGR designs. While nuclear power is essentially free of emissions from carbon combustion during normal operation, the reaction of carbon, in the form of graphite, with molecular oxygen is still an important consideration in the event of an extremely unlikely pressure boundary leak or break accident followed by air ingress into an HTGR. This being said, the reaction of graphite with oxygen is not the same as that of coal burned in a coal-fired power plant. Although graphite will oxidize rapidly in air at high temperatures, graphite oxidation is not self-sustaining, in other words, it does not burn. Upon removal of the heat source and/or the oxidizing gas (oxygen), the reaction cannot continue. This is in part due to the fundamental differences in chemical bonding as well as the additional elements and impurities that exist within many other carbonaceous materials. The miscorrelation of coal in a power plant or briquettes for a charcoal grill has led to the incorrect assumption that graphite is capable of burning in an air ingress incident [4, 5].

### 2.1.1. Relevant Air Oxidation Scenarios

The relevant air ingress scenarios of interest for an HTGR may vary significantly based upon the regulating body, design type, and reactor size, but also in terms of severity. Regardless of the accident scenarios of interest, air ingress involving a compromised pressure boundary in an HTGR should be considered an off-normal event. There are several plausible, yet highly unlikely design basis accidents (likelihood between $10^{-2}$ and $10^{-6}$ events per plant year) that can be considered for future licensing applications. While acute graphite oxidation in air will likely never occur during an HTGR's licensed lifetime, it is important to understand such events as they have the potential to cause significant changes to the geometry of cooling channels, graphite density, mechanical strength, and graphite thermal properties.

Air ingress may occur following a break in the pressure boundary and the resultant depressurized loss of forced circulation (D-LOFC). In a D-LOFC accident, an HTGR's core temperature will begin to heat up due to the loss of coolant, and a mixture of helium and air will enter the reactor at very low velocities over an extended period ranging from several hours to days. Once a critical amount of air has displaced the coolant helium, natural convection will become the dominant oxygen transport process within the reactor [6,7]. The following phenomena must be considered:

1. Oxidation of graphite structures to the extent that the core and/or its supports become structurally compromised.

2. Oxidation of graphite fuel elements leading to:

    a. Exposure of fuel particles (tristructural-isotropic particles) to oxygen; potentially followed by

    b. Release of fission products (if the silicon carbide layer becomes compromised).

3. Release of fission products that had previously been strongly adsorbed by graphite components and other core structures.

While all three points are important to consider, further discussion will be limited to considerations of the graphite structures within an HTGR.

### 2.1.2. Oxidation Inputs for Simulation and Design

Simulation of air ingress accidents is typically performed for the deterministic safety analysis report, which accompanies a nuclear license application to the regulating authority. The analysis is used to determine the structural integrity of the graphite supports and to provide information on the possible radionuclide releases that could accompany these events. Modeling efforts currently use the observed graphite oxidation rate to assess strength. The rate is integrated over the life time of the simulation to obtain total mass loss for a graphite component: with the existing approach, the microstructural changes (intrinsic to the evolution of graphite performance with oxidative mass loss) are not specifically considered.

A typical air ingress simulation consists of three physics modules coupled together and solved in iterative (explicit) or simultaneous (implicit) schemes. The three modules are:

- *Heat source*. The heat source module is primarily a neutronics module to calculate the total heat produced from fission product decay and fission processes. When appreciable amounts of moisture or steam are involved, this module must also account for the increase in fission power. The heat of reaction from the exothermic graphite-oxygen reaction is also considered in this module.
- *Graphite-oxygen reaction*. The graphite-oxygen reaction module extrapolates the rate of oxidation along the length of graphite structures within the core, such as the graphite fuel blocks and reflector blocks as well as the core supports. The primary inputs are the gas composition along the length of the reactor component (from the thermal fluids module) and temperature of the graphite (from the heat source module). The graphite-oxygen reaction module currently relies upon graphite-specific kinetics models empirically derived from the observed oxidation rates of relatively small specimens.
- *Thermal fluids*. The thermal fluids module accounts for both mass and heat transport in and out of the reactor by the various a number of transport routes. This module interacts with the graphite-oxygen reaction and heat source modules to resolve parameters spatially, such as temperature, gas velocity, and gas composition. It is also fundamental to determining other local gas properties, such as density, viscosity, and thermal conductivity, pertinent to the conservation of energy and mass in the system.

The outcomes of this process are “maps” of graphite temperatures and graphite oxidation rates in all affected regions. The observed oxidation rates can then be integrated over the duration of an air ingress accident to determine total mass-loss for various components. It should be stressed that not all regions in the core are equally important in terms of the consequences of graphite oxidation events. If the graphite oxidation is limited to the inner or outer reflector blocks for example, the main concern would be to assess whether the control rods can still be inserted to

ensure core shutdown after an ingress event, and oxidation of the bottom support structures likewise carries minimal radiological risk. However, the structural integrity of the bottom graphite support columns must be assessed during and after air ingress to ensure that sufficient safety margins remain.

## 2.2. Current Oxidation Kinetics Models

Graphite oxidation in an accident scenario is not in-and-of-itself a real concern, rather the issue is the microstructural change inflicted. The microstructural change in turn degrades the physical, mechanical, and thermal properties of the graphite. One example may be the reduction of mechanical strength after oxidation causing concerns regarding the structural integrity of a graphite component. Given this, the logical question is not how much oxidation occurs under a given set of conditions, but rather how much microstructural damage can be tolerated before there is an unacceptable risk of component failure? Or, based on a specific accident scenario, a more relevant question may be how long a load-bearing graphite component can last before it fails?

Traditionally, nuclear graphite oxidation kinetics models have been derived almost entirely from measurements of the mass loss versus time for relatively small specimens. The sample size has depended mostly on practical constraints of the experimental equipment used. The rate equations, almost without exception, have been semi-empirically fitted with a classic Arrhenius temperature dependence:

$$rate = k_0 e^{-\frac{E_A}{RT}} {P_{O_2}}^n \quad (1)$$

and an occasional use of the slightly more pedantically correct form [8, 9].

$$rate = k_0 e^{-\frac{E_A}{RT}} [O_2]^n \quad (2)$$

In either case, $k_0$ is a pre-exponential factor, $E_A$ is an activation energy, and n is the reaction order. These parameters are more adequately described as observed parameters (see terminology section) since most experimental data collected does not purely represent the so-called “kinetics regime.” Rather, most experimentally derived kinetics models naturally convolute the inherent reaction kinetics, with the individual graphite grade’s specific mass and heat transfer characteristics. In the past, this simple method has worked for estimating the total mass loss of experimental samples of a specific graphite grade under specific conditions, but at the very least it is overly conservative.

Furthermore, the increased sophistication in multi-physics computer modeling and the heightened safety concerns worldwide have led the governing regulatory bodies as well as reactor designers to ask questions that are more specific and require more detailed answers regarding a candidate graphite’s oxidation performance. Unfortunately, the answers to these

more sophisticated questions require highly non-trivial solutions and the answers are highly dependent on multiple factors. Our simple past methodology may not provide adequate answers to these specific questions for a wide range of accident scenarios.

### 2.3. Limitations of Current Kinetics Models

The following two engineering examples are meant to draw attention to some of the drawbacks in the current semi-empirical kinetics models. Fig. 1 shows compressive load test results for multiple graphite specimens oxidized to 10% mass loss for a single graphite grade. The unoxidized sample had a failure load slightly greater than 60 MPa. Three samples were oxidized to 10% mass loss at 640°C, 689°C, and 739°C. While each sample has lost an identical fraction of their initial mass during oxidation, the compressive strength results do not have an obvious correlation with the % mass loss. At the lower temperatures, 640°C and 689°C, the compressive strength decreases to <50% of their unoxidized counterpart, while the compressive strength of the sample oxidized at 739°C retains nearly 70% of its unoxidized compressive strength.

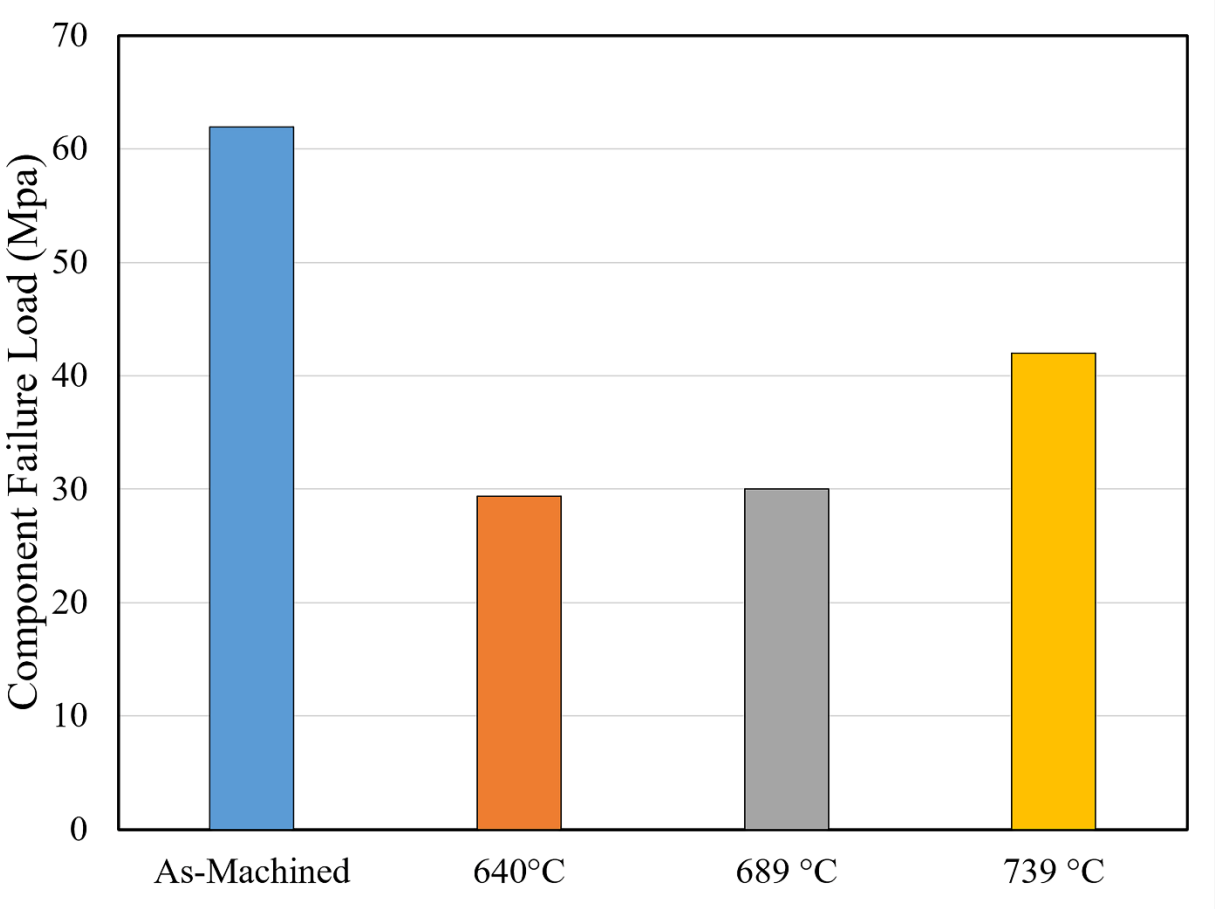


**Fig. 1.** Failure load measurements are shown for four different conditions. The as-machined samples were tested after machining without exposure to oxidizing conditions. The remaining samples were oxidized to 10% total mass loss at the temperatures designated in the plot. All

samples were originally machined as right cylinders with a length of 5.08 cm and a diameter of 2.54 cm.

Similar results have been shown in the graphite literature for some time [10-15] and the trend is not surprising. An explanation of these results is fairly intuitive upon considering the chemical reaction as well as mass transport. At lower temperatures, the chemical reaction is slow compared to the rate of gas transport into and out of the sample and oxygen can effectively travel deep into the specimen before it is consumed by the chemical reaction at a pore surface. As a consequence, oxidation is fairly uniform throughout the sample and the percentage mass loss accurately represents the amount of oxidation that has taken place throughout the interior of the sample. This is visually shown on the right side of Fig. 2. Fig. 2 is a slight modification of the classic figure by Walker et al. seen repeatedly throughout the nuclear graphite literature [16]. Obviously from Fig. 2, at the higher temperature (739°C), the chemical reaction is exponentially faster and the transport of oxygen relatively slow in comparison. This severely limits the depth oxygen can penetrate into the sample and as a result, effectively limits oxidation to a thin region near the sample exterior while the interior remains relatively unaffected by oxidation. In the extreme (hypothetical) case where the chemical reaction is infinitely faster than the rate of diffusion, oxidation occurs only at the exterior surface of graphite and does not penetrate at all into the graphite. This is shown at the extreme left of Fig. 2. For the sample oxidized to 10% mass loss at 739°C, the effective diameter has been reduced to approximately 2.41 cm. Similar compressive strength results would have been achieved by testing an unoxidized sample with a diameter of 2.41 cm and normalizing the test results to an effective diameter of 2.54 cm.

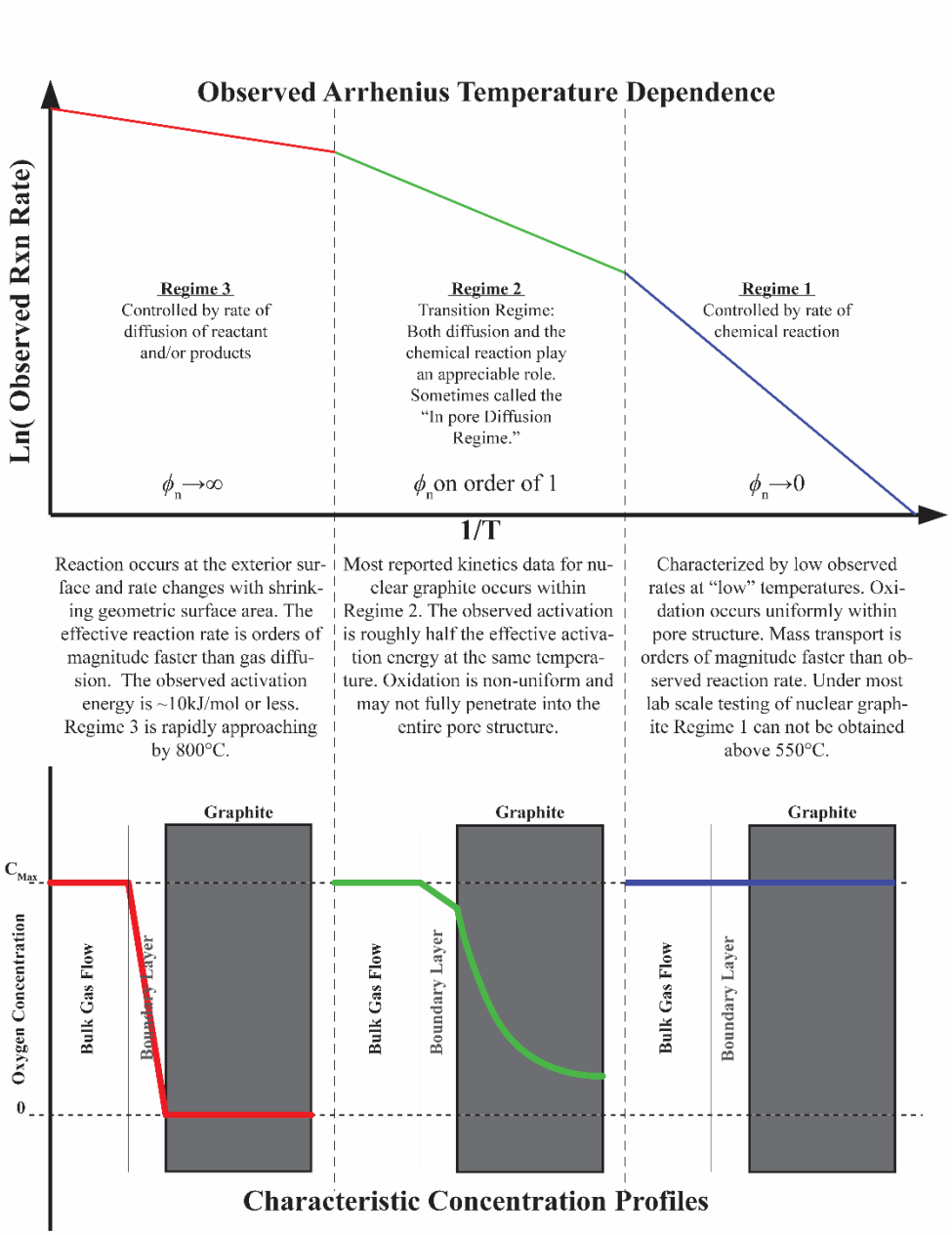


**While temperature is a substantial factor in determining the regime experimental data may fall within other factors include such as sample size, geometry, gas flow rate, and microstructure.*

***The ideal Regimes 1 and 3 depicted in the characteristic concentration profiles can be thought of as the upper and lower bounds of the Thiele modulus. In reality all experimental data lies somewhere between these two extremes.*

**Fig 2.** A classic figure showing the two ideal extremes governing the oxidation kinetics of catalysts and porous materials. For most oxidizing environments relevant to a HTGR, the observed rate will be controlled by chemical reaction and mass transfer simultaneously. The oxygen profiles in the lower half of the figure have a strong temperature dependence, but the curves can shift significantly by varying oxygen concentration, interfacial gas velocity, the inherent microstructure, and the geometry and size of the graphite.

While these results are easily explained qualitatively, our current oxidation kinetics models by themselves cannot predict the effective depth of oxygen corrosion, and thus cannot predict the obviously important role that gas transport plays in nuclear graphite oxidation within full-sized graphite components.

Expanding beyond a single graphite grade, Fig. 3 provides a glimpse into further limitations of current oxidation kinetics models. The first and perhaps most obvious is, under identical conditions, each graphite grade oxidizes at a significantly different rate. At 1% mass loss, there is a spread of nearly 3 hours. For 5% mass loss, the time difference between the slowest and fastest oxidizing samples more than triples to almost 10 hours. By 10% mass loss the time to oxidize the slowest oxidizing grade is nearly 300% longer than the time needed to oxidize the fastest oxidizing grade. The different oxidation rates can be attributed to differences in microstructure (primarily pore structure) and the types of surfaces available for each grade. Current oxidation kinetics models are not microstructurally informed and therefore cannot predict the oxidation rate of multiple graphite grades. At first, this may seem like a minor issue as experimental tests can be performed over a wide range of controlled conditions, but carbon material properties, including oxidation, are highly dependent on the initial carbon precursor materials and their processing. A graphite grade may be developed and optimized for use in an HTGR using a particular precursor carbon source, but by the time the reactor is actually built, a new carbon precursor source may be needed. While the same manufacturing process would be used and the precursor could be selected to closely resemble the former, the new carbon source material(s) could still affect the oxidation performance.

Next, the instantaneous oxidation rates, represented by the slope of the mass-loss curves in Fig. 3, vary significantly with increasing oxidation time. In a broad sense, the oxidation rate changes due to continuous microstructure change as carbon atoms are perpetually removed from the surfaces of pores in the sample interior as well as the exterior surface. Current kinetics models are not time dependent and do not consider the evolution of graphite microstructure over time. ASTM D7542-09 avoids this issue by disregarding the rapidly increasing “onset” rate data in favor of a more rapid, more nearly constant rate evaluated over a later mass loss interval. This convention favors evaluation of a more reproducible, but consequently extremely conservative, observed oxidation rate over any attempt to address the time dependence (or conversion, $\alpha$, dependence) of oxidation.

Finally, current semi-empirical fits of rate data are collected for relatively small samples compared to full scale graphite components. Rate information is often normalized on a mass, volume, or perhaps even exterior geometric surface area basis. When scaling to a full-sized monolithic graphite component, one must at least question how well the established model applies to a larger component.

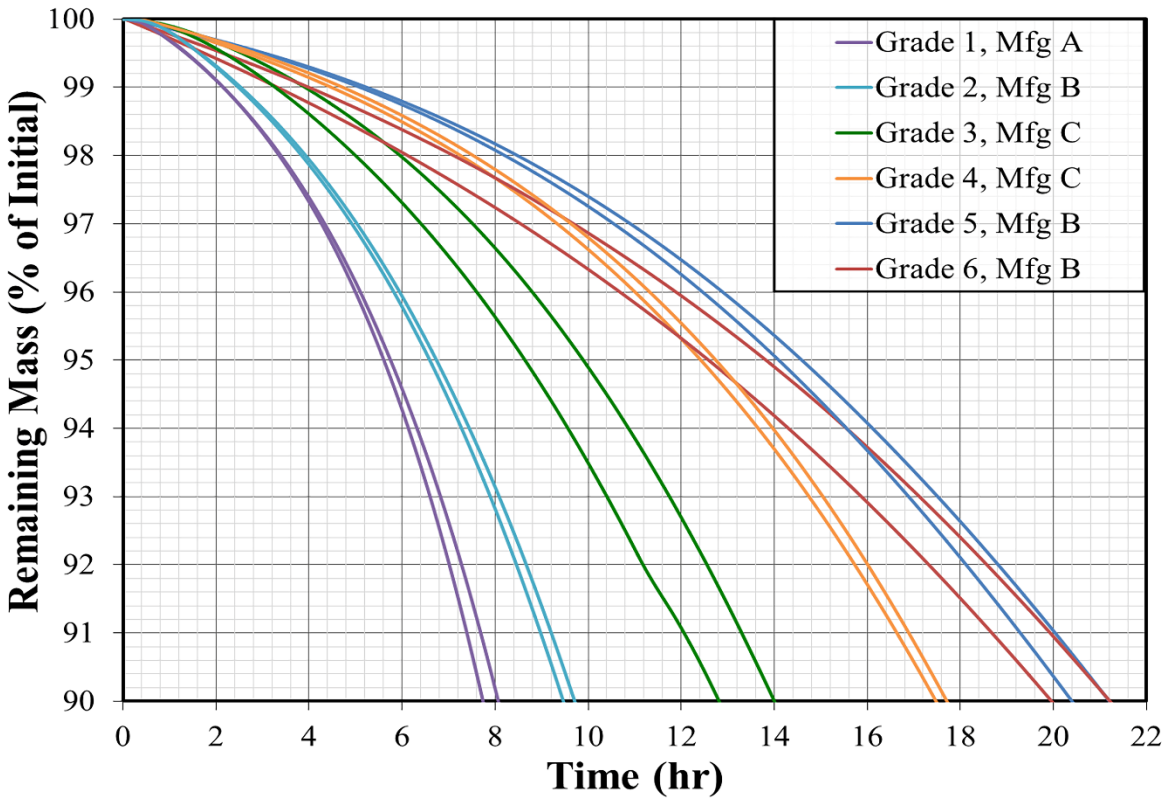


**Fig. 3.** Mass loss is plotted as a function of time for six different graphite grades. All samples were oxidized at 640°C in air following ASTM standard D7542-09. All samples were right cylinders with a length of 5.08 cm and a diameter of 2.54 cm.

While we, as a research community, have a good qualitative understanding of the phenomena behind the observed trends shown above, our current oxidation kinetics models alone are not conducive to quantification of these phenomena. Mass transfer and heat transfer as well as the microstructural evolution of a graphite must also be taken into account in order to account for the observed phenomena. In summary our current kinetics models for oxidation:

4. Cannot predict how far microstructural damage will penetrate into a specimen, which affects its mechanical strength (Fig. 1) as well as physical and thermal properties.

5. Cannot account for different rates due to a different manufacturing process, source material, or filler particle size. In other words, each kinetics model is grade specific (Fig. 3).

6. Do not consider the changing microstructure as oxidation progresses.

In light of the increased level of certainty needed by design engineers to meet more specific criteria during hypothetical accident scenarios set forth by governing regulatory bodies, our current oxidation kinetics models seem somewhat incomplete. This is largely due to the fact that they are designed around observable measurements of the rate of mass loss rather than the

intrinsic features that dictate the performance of a particular graphite. If our oxidation models need to meet the current demands placed upon them for extreme environments of newer HTGR designs, it is perhaps time to consider a fundamental change in how we approach graphite oxidation in the nuclear field.

## Article Overview

The remainder of this article is divided into four sections. Section 3 will begin with a brief summary of the assumptions needed for an improved oxidation model based on an intrinsic reaction rate. It will then discuss the graphite-oxygen reaction mechanism and provide a preliminary intrinsic reaction model for graphite oxidation.

Section 4 will begin with a description of the various length scales from the atomic to macroscale that give each grade a unique effective reaction rate. It will then introduce how mass transfer affects the observed rate of oxidation measured in experimental tests as well as the effects of a continuously evolving pore structure. This section will briefly discuss the more obvious effects of mass transport as shown in the transition region of Fig. 2, but will also discuss more subtle features that are often overlooked or ignored in the nuclear graphite literature.

Section 5 will build upon Sections 3 and 4 to provide the equations for the effective reaction rate, mass and energy conservation, and boundary conditions governing the observed rate of graphite oxidation keeping in mind the intrinsic chemical reaction rate. The majority of this section will focus on the identification and physical meaning of microstructurally based parameters needed to describe the unique observed oxidation rate of each graphite grade.

Finally in Section 6, several key research areas will be discussed highlighting current areas of research that would further benefit the development of a model similar to that proposed in Section 5.

# 3. The Graphite-Oxygen Reaction Mechanism

### 3.1. Assumptions of an Intrinsic Reaction Model

To develop an intrinsic reaction model, three critical assumptions are needed. First, at the atomic level, high-purity nuclear graphite grades must be considered indistinguishable having identical crystallographic and chemical structure. If each graphite has the same structure on the atomic scale, the chemical reaction should be identical at some fundamental level and a single-rate equation may be used to describe the rate of chemical reaction for each nuclear graphite grade if the rate is properly normalized (An oxidation kinetics model for all nuclear graphites oxidize in an molecular oxygen environment). This normalization will be discussed in more detail in Section 3.3.

Fig. 4 shows qualitative evidence partially supporting this assumption, at the nanoscale, with high-resolution transmission electron micrographs of three nuclear graphite grades. Independent of grade (Fig. 4a-c) and whether filler or binder-matrix material is examined, each has the same

atomic structure. The authors are well aware that despite graphitization at temperatures approaching 3000°C, a small fraction of the synthetic graphite will not be fully graphitized (mesophase material). In Section 3.2 we will briefly reason that even this small fraction will, in terms of oxidation, react at a nearly identical intrinsic rate to the fully graphitized material.

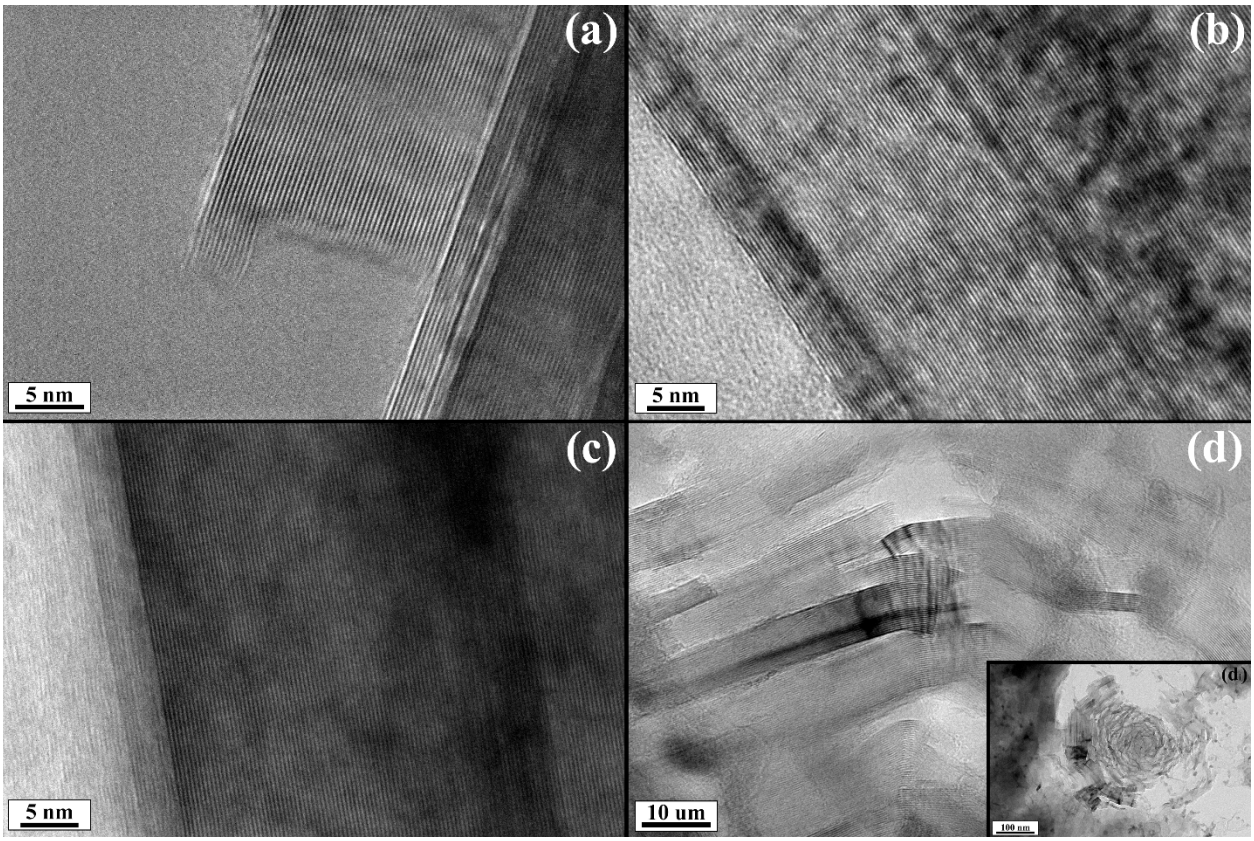


**Fig. 4.** Four high-resolution transmission electron micrographs of three nuclear-grade graphites are shown. These grades are designated IG-110 (Fig. 4a), PCEA (Fig. 4b), and NBG-18 (Fig. 4c and d) by their respective manufacturers. Figs. 4a–c are micrographs of filler material. Fig. 4d shows oxidized NBG-18 binder. The inset of Fig. 4d shows the location of the main micrograph within a partially oxidized quinoline insoluble particle.

Second, it is assumed that graphite is porous and has an open-pore structure. An open pore is defined here as a pore that may be accessed by a gas molecule without changing state. In other words, a physical process such as surface diffusion or solid-state diffusion is not necessary to reach an open pore. Consequently, we assume here that all oxidation occurs at the surface of open pores and to a lesser degree at the exterior surface of the tested graphite specimen.

The final, third, assumption is made in regards to impurities. Nuclear graphites are considered high-purity graphite, but inevitably impurities do exist. American Society for Testing Materials (ASTM) standard D7219 defines high-purity nuclear graphite as having an ash content below 300 ppm and an equivalent boron content of less than 2 ppm; however, many modern nuclear

graphites have significantly lower impurity levels on the order of 10 ppm due to high-purity graphite needs in the semiconductor industry [17]. Locally, metallic impurities may catalyze oxidation by activating $O_2$ on the surface of the impurity. Oxygen is subsequently transferred to carbon via surface migration at a high efficiency, which locally increases the oxidation rate in the vicinity of the impurity. Given the low level of impurities, catalytic oxidation is assumed here to have no appreciable effect on the intrinsic oxidation rate when averaged over all active carbon sites. Instead, it is assumed that impurities affect nuclear graphite oxidation by gradually increasing the active surface area through channeling, pitting, or tunneling [18], or a combination of the three as the reaction proceeds. This gradual increase in active surface area is assumed here to be an inherent characteristic of the graphite grade.

### 3.2. Reaction Mechanism

The graphite-oxygen reaction mechanism is fairly complex. To fully appreciate the complexity a basic understanding of the graphite crystal structure and its chemical anisotropy is needed. Graphite has strong directional covalent $sp^2$ hybridized bonding within the carbon basal planes, (002), and weak delocalized $\pi$ bonds between planes making the interactions between planes quite weak (Fig. 5a). Since the interaction between layers is weak, the graphite-oxygen reaction can be adequately described using a single layer of carbon atoms, also known as the novel two-dimensional (2D) material, graphene.

Due to the strong covalent nature of the carbon bond within graphene (basal plane of graphite), oxygen has a high affinity for "unsaturated" carbon atoms at the edge of the plane $(hk0)$ [19], specifically chemisorption of oxygen takes place on activated sites such as carbene-like zig-zag and carbyne like armchair sites [20]. These sites are illustrated in Fig. 5b. Conversely, the interior carbon atoms of graphene are inert to molecular oxygen. Adsorption, both molecular and dissociative, does not occur and has been shown to be highly unfavorable thermodynamically at these interior lattice sites [19, 21].

Returning to the first assumption of Section 3.1 to elaborate, the graphite chemical structure is indistinguishable among graphite grades in this regard. Borrowing heavily from Montoya et al., most high purity, ungraphitized, carbon materials have structures consisting of very small randomly connected graphene sheets [22]. Even a high-purity char for example, has graphene clusters containing 12–25 aromatic carbon atoms [23]. Electrons do not delocalize through single bonds efficiently; and consequently, for the much larger nuclear graphite crystallite it is fairly safe to assume that the surrounding environment (other crystallites) does not significantly impact the reactivity. Does the size of a graphene sheet have an impact on the reactivity? Multiple research groups have shown via simulation that graphene reactivity does not strongly depend on the size of the graphene molecule after it has reached a size of approximately 50 carbon atoms [24, 25]. A more important parameter, that will briefly be discussed in Section 3.5, is the local topology of the active site (zig-zag or armchair), as shown in Fig. 5b and the surrounding surface intermediates. For the remainder of this article, with the exception of the discussion in Section

3.5, we rely upon the assumption that all nuclear-grade graphites have identical chemical structure and, therefore, identical intrinsic reactivies with oxygen.

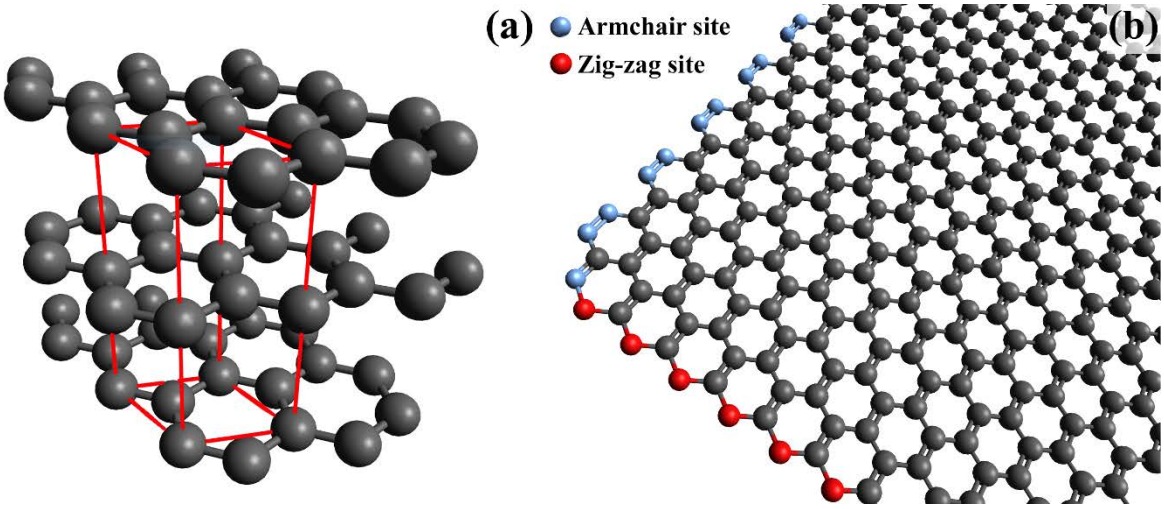


**Fig. 5.** Crystal structure of graphite and its unit cell (outlined in red). Fig. 5b shows the edges of a graphene sheet highlighted as blue or red atoms. The red sites represent carbene-like zigzag sites in the (11) plane and the blue sites represent carbyne-like armchair sites in the (10) plane. Oxidation via molecular oxygen occurs predominantly at these two types of edge sites.

As stated previously, the graphite-oxygen reaction mechanism is exceptionally complex [18, 26]. Taking into account all known influential factors is beyond the aim and scope of this article. A reasonably simple, yet arguably necessary and sufficient oxygen transfer mechanism based primarily on the work of Radovic et al. [20, 21, 27, 28] is described here with some simplification [29].

Eq. (3) shows the deceptively simple overall reaction between molecular oxygen and carbon.

$$C(s) + \left(1 - \tfrac{1}{2}x\right)O_2(g) \rightarrow xCO(g) + (1-x)CO_2(g) \tag{3}$$

The oxygen transfer mechanism below presents the same overall reaction in terms of intermediate reactions. A visual schematic of the oxygen transfer mechanism is shown in Fig. 6.

$$C_e + O_2(g) \xrightarrow{k_{A1}} C_e(O_2) \qquad \text{Molecular Oxygen Chemisorption} \tag{4a}$$

$$2C_e + O_2(g) \xrightarrow{k_{A2}} 2C_e(O) \qquad \text{Oxygen Dissociative Chemisorption} \tag{4b}$$

$$\mathrm{C_e(O_2) + C_b \xrightarrow{k_S} C_e(O) + C_b(O)} \qquad \text{Oxygen Spillover} \tag{5}$$

$$\mathrm{C_{b1}(O) + C_{b2} \xleftrightarrow{K_{Hop}} C_{b1} + C_{b2}(O)} \qquad \text{Surface Diffusion/Oxygen Migration} \tag{6}$$

$$\mathrm{C_e(O_2) \xrightarrow{k_{D1}} CO_2(g) + 2C_e} \qquad \text{Direct CO2 Desorption} \tag{7a}$$

$$C_e(O) + C_b(O) \xrightarrow{k_{D2}} CO_2(g) + 2C_e \quad \text{Indirect CO2 Desorption} \quad (7b)$$

$$C_e(O) \xrightarrow{k_{D3}} CO(g) + 2C_e \quad \text{Direct CO Desorption} \quad (7c)$$

$$2C_e \xrightarrow{k_{NSD}} 2C_b \quad \text{Nascent Site Deactivation} \quad (8)$$

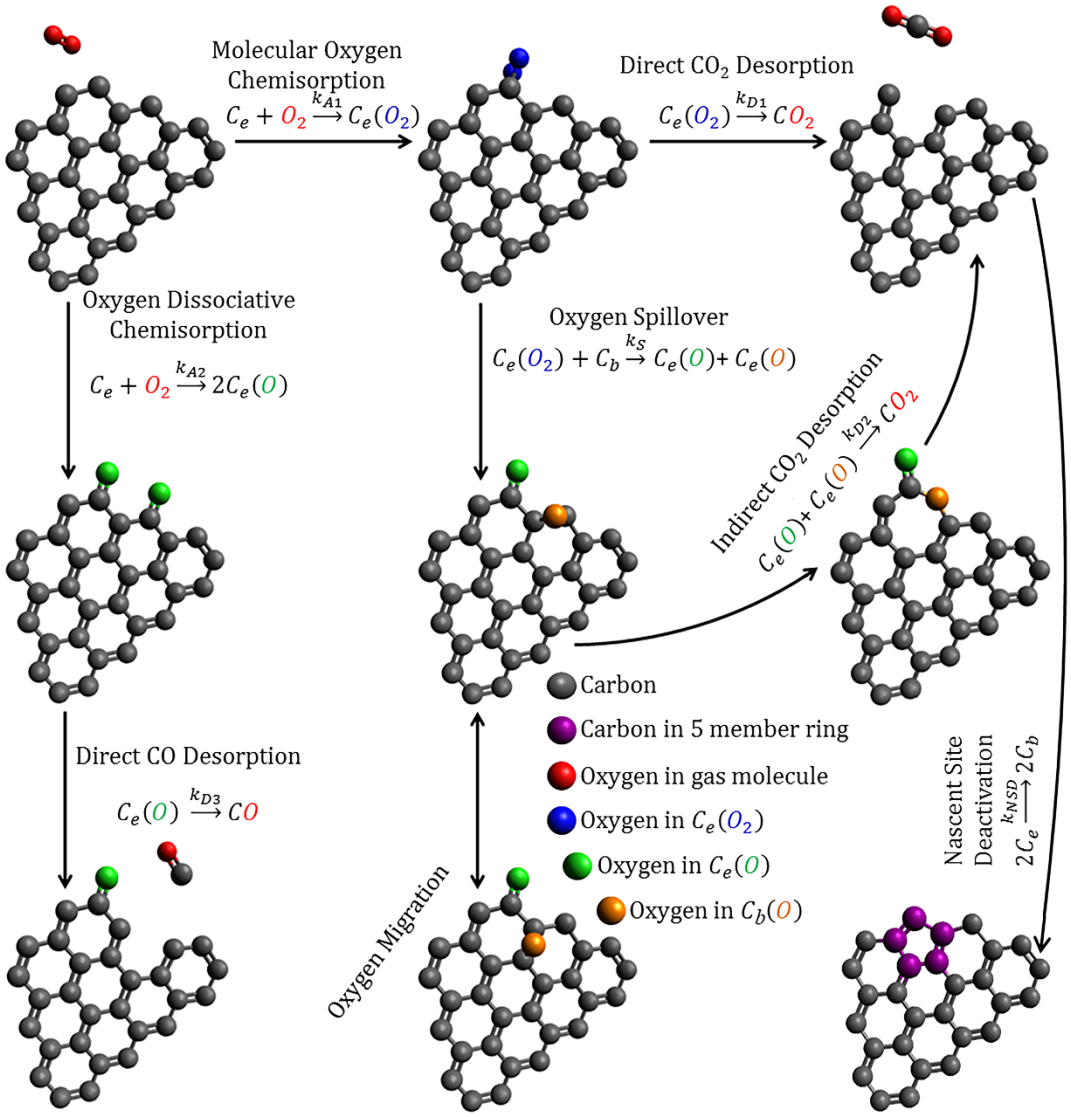


**Fig. 6.** The mechanism for the reaction of graphite with molecular oxygen. This figure visually illustrates Eqs. (4–8).

Starting at the top left-hand corner of Fig. 6, when molecular oxygen comes in close proximity to the edge of a graphene sheet (zigzag or armchair sites, denoted ambiguously here as $C_e$), molecular or dissociative chemisorption may occur by the reactions represented in Eqs. (4a) and (4b), respectively [28, 30]. The reactive dioxyranyl intermediate, $C_e(O_2)$, and reactive

semiquinone intermediate, $C_e(O)$, can both undergo direct desorption to produce $CO_2(g)$ [31, 32] and $CO(g)$ [18] via Eqs. (7a) and (7c), respectively.

After molecular chemisorption, atomic oxygen is also capable of spilling over onto the basal plane producing an epoxide, $C_b(O)$, "stable" intermediate and leaving a $C_e(O)$ on the graphene edge [17, 29]. $C_b(O)$ is typically labeled as stable in the oxidation literature because it is incapable of direct desorption from the basal plane [15]. The stable intermediate plays two critical roles in the reaction mechanism. First, indirect desorption of $CO_2(g)$, represented by Eq. (7b), occurs when $C_b(O)$ is able to diffuse (Eq. [5]) to a site on the basal plane adjacent to a semiquinone, the oxygen atom is inserted into the carbon ring and desorption of $CO_2(g)$ ultimately occurs [32, 34]. The indirect path for $CO_2(g)$ desorption is predominant at low temperatures $\lesssim 1100°C$, whereas the direct desorption process only becomes significant, relative to the indirect path, at higher temperatures [31, 35].

$C_b(O)$ has also been shown, via density functional theory simulations, to reduce local carbon-carbon bond strength by approximately 30% [36]. As cleavage of the carbon-carbon bond is the major energy barrier for desorption of $CO(g)$ and $CO_2(g)$, the presence of $C_b(O)$ drastically affects the respective activation energies for desorption.

The final step of the oxygen transfer mechanism takes place after desorption has occurred. Upon removal of a carbon atom from the graphene sheet, two highly activated, nascent, sites are left behind. Left undisturbed, these sites will deactivate through the formation of a more stable and certainly less-reactive five member ring. However, in a reacting system there is always an ongoing competition between further oxidation of these sites and their deactivation [27, 37, 38]. For more detailed summaries of key contributions and findings to the underlying graphite-oxygen mechanism over the past half century, the reader is referred to the vast amount of authoritative literature on the subject of carbon oxidation [18, 27, 29, 30, 39-45].

### 3.3. Surface Area Classifications

From the discussion above, it is quite apparent, in terms of reactivity, that distinctly different types of carbon sites exist. Three sites are commonly distinguished in the carbon oxidation literature as different types of surface area. The first is total surface area (TSA). TSA encompasses all carbon atoms at a gas-solid interface. TSA is typically evaluated by the BET surface area from $N_2$ adsorption at 77 K. The next two classifications are subsets of TSA termed active surface area (ASA), and reactive surface area (RSA). ASA is the portion of TSA that is capable of oxygen chemisorption. In Fig. 5b, ASA encompasses the 17 carbon atoms (11 blue and 6 red) that make up the visible edge of the graphene sheet. In a perfect, defect-free, graphene sheet or graphite single crystal, the edge sites of any graphene plane are the only active sites. RSA is a subclass of ASA in that it is defined as the subset of sites within ASA that are part of a reactive intermediate. In literature, RSA is typically stated for a given set of conditions; thus, a pseudo-steady state is implicitly assumed [19, 46, 47].

Fig. 7 visually illustrates the differences between the sites belonging to each classification of surface area. There are 98 carbon atoms shown within the graphene sheet. All 98 carbon atoms are considered part of the TSA as they are all at the gas solid interface. Of the 98 carbon atoms, only 10 are shown along the edge of the sheet. These 10 sites have already or are capable of chemisorption of oxygen. Therefore, these sites are active sites and may be designated as ASA. Six of the 10 carbon atoms within the ASA are part of a semiquinone or dioxyranyl reactive intermediate. These six atoms may be classified further as reactive sites and designated as RSA. The carbon atoms within the basal plane with oxygen attached are not considered to be ASA or RSA because the attached oxygen is not there as a result of chemisorption but rather the spillover of oxygen from the edge sites and have migrated from the edge to their current location. Furthermore, they cannot directly desorb from the basal plane.

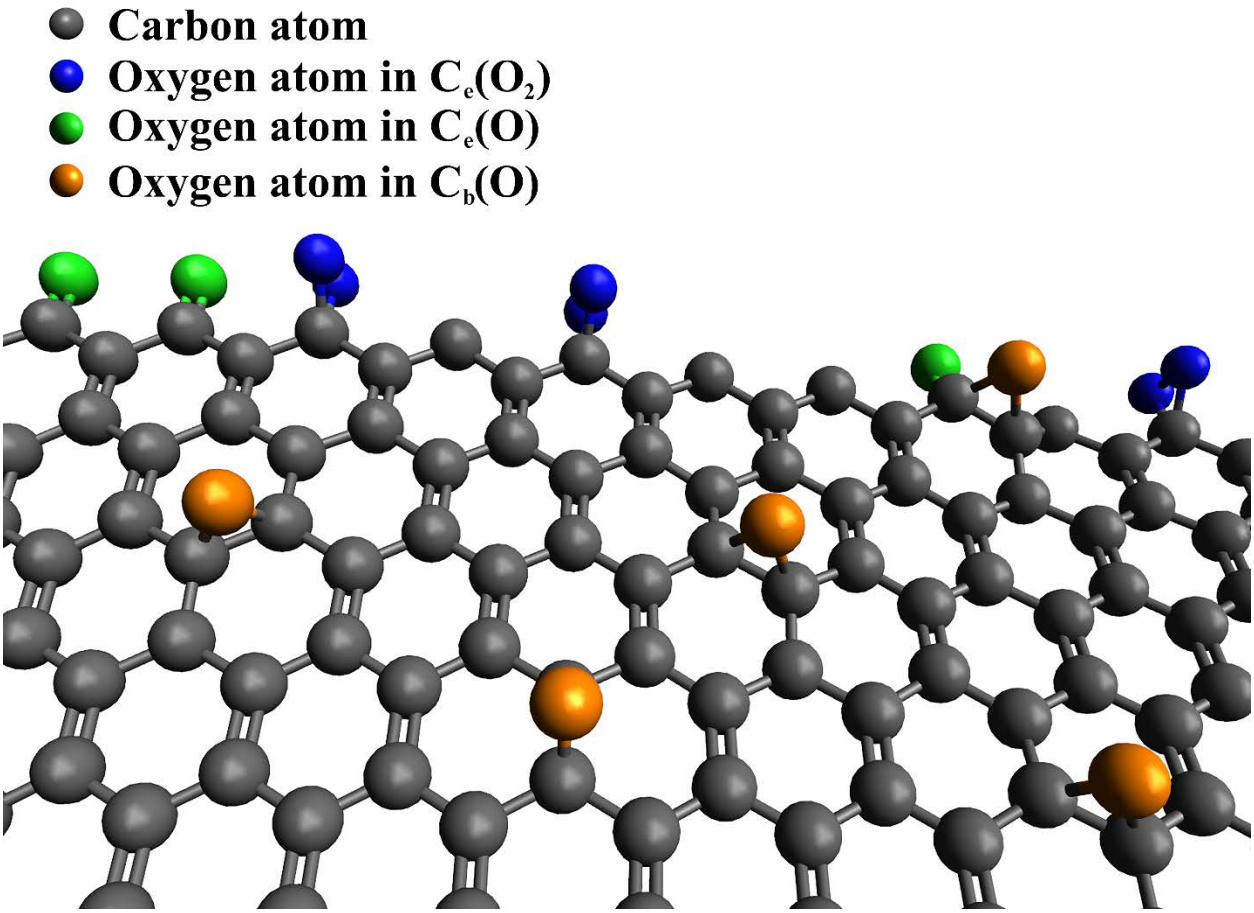


**Fig. 7.** Carbon site classifications and the three different surface intermediates.

The intrinsic rate of oxidation is tied directly to the surface densities (surface concentrations) of the two reactive intermediates; therefore, an intrinsic rate must be normalized to a particular graphites RSA. There are several barriers to a true normalization of the reaction rate to the RSA of a particular graphite. The first being RSA will vary substantially with environmental variables, such as temperature and oxygen concentration. The second being RSA is not easily

measured. Even when a measurement is made, interpretation of its physical meaning is not always straightforward [19, 46, 47].

If a relation for surface coverage as a function of temperature and oxygen concentration can be established,

$$\theta = {RSA}/{ASA} \tag{9}$$

an intrinsic reaction rate could effectively be normalized to ASA instead, which may be easier to quantify and is certainly more intuitive to understand. In the following section a model will be presented that essentially establishes an approximation for this relationship.

The importance of distinguishing between the three surface types, as well as normalizing to RSA for real, non-ideal graphite materials will be discussed in Section 3.5.

### 3.4. Oxygen Transfer Model

Assuming Eqs. (4–8) may be treated as elementary reactions, Eq. (10) is the rate of carbon consumption for **any** high purity graphene or graphite material if the flux is normalized to the material's RSA.

$$-N_C = k_{D1}^*[C_e(O_2)] + k_{D2}^*[\mathrm{C_e(O)}] + k_{D3}[\mathrm{C_e(O)}] \tag{10}$$

The first two terms represent the production rate of $\mathrm{CO_2(g)}$, from the direct and indirect paths, respectively (Eqs. [7a] and [7b]). The third represents the formation rate of $\mathrm{CO(g)}$ (Eq. [7c]). While this rate law may be theoretically useful and can provide insight into many common trends observed in the oxidation literature, it has no practical value on its own since the concentration of surface intermediates are not easily determined and are not conducive to direct experimental measurement. A rate equation in terms of $\mathrm{O_2(g)}$ concentration is much more favorable as measuring $\mathrm{O_2(g)}$ concentration is extremely simple compared to measuring concentrations of surface intermediates. The surface concentrations of the intermediates may be expressed in terms of molecular oxygen concentration through the use of differential mass balances about the ASA, expressed here as $C_e$, and the reactive intermediates $C_e(\mathrm{O})$ and $C_e(O_2)$, which make up the RSA [29].

Following the derivation and assumptions of Kane et al [29], Eq. (10) becomes the oxygen transfer model (OTM). $\Gamma_e$ is the active site surface density in moles per unit active surface area ($\mathrm{mol/m^2_{ASA}}$).

$$-N_C = \frac{\left(k_{A1}k_{D1}^* + (k_{A1}+k_{A2})\left(k_S^*+k_{D1}^*\right)\right)(k_{D2}^*+k_{D3})\Gamma_e[O_2]}{(k_{A1}+k_{A2})(k_S^*+k_{D1}^*)[O_2] + \left(k_{A1}[O_2]+k_S^*+k_{D1}^*\right)(k_{D2}^*+k_{D3})} \tag{11}$$

The OTM, at first glance, may seem complex, but defining an effective reaction rate constant, $k_{eff}^{"}$, and assuming each rate constant from Eqs. (4–7) have an Arrhenius temperature dependence, Eq. (11) becomes:

$$-N_C = k_{eff}^{"}(T, [O_2])[O_2] \tag{12}$$

where

$$k_{eff}^{"}(T, [O_2]) = \frac{\left(k_{A1}k_{D1}^{*} + (k_{A1}+k_{A2})(k_S^{*}+k_{D1}^{*})\right)(k_{D2}^{*}+k_{D3})\Gamma_e}{(k_{A1}+k_{A2})(k_S^{*}+k_{D1}^{*})[O_2] + (k_{A1}[O_2]+k_S^{*}+k_{D1}^{*})(k_{D2}^{*}+k_{D3})} \tag{13}$$

A quick comparison reveals that Eqs. (2) and (12) are nearly identical , when the reaction order in Eq. (2) is assumed to be one, differing only in terms of rate normalization. Eq. (2) is typically normalized to an easily measureable extrinsic property such as mass, while Eq. (12) is an intrinsic rate since it is normalized to RSA. For Eq. (12) and Eq. (13), RSA is defined implicitly by the elementary reaction coefficients and approximates the surface coverage as a fraction of $\Gamma_e$. Normalization to RSA is critical to the development of an intrinsic oxidation model capable of determining observed oxidation rates for any nuclear graphite.

### 3.4.1. Advantages of the Oxygen Transfer Model

While Eq. (11) is certainly more cumbersome than the traditional semi-empirical rate equation commonly used, it offers some distinct advantages. The most important being Eq. (11) removes any dependency of the chemical reaction rate on a graphite's microstructure allowing the use of a single intrinsic reaction rate for all grades. This advantage is quite powerful as it opens up the possibility of predicting observed oxidation rates based solely on the inherent structural properties of various graphite grades for any combination of gaseous environmental parameters (temperature, oxygen concentration, flow rate, etc.). The modeling and experimental work needed to achieve this will be discussed in Sections 5 and 6.

### 3.4.2. Dependence of effective parameters on temperature and oxygen concentration

Based on Eq. (13), one would expect the effective reaction order, the effective reaction rate constant, and/or the effective activation energy (depending on the semi-empirical form chosen) to vary with temperature and to a lesser extent with oxygen concentration. The OTM describes the effects of temperature and oxygen concentration on the effective reaction rate, so that the appropriate values can be used in Eq. (2) and used to describe the reaction kinetics of graphite over several small ranges of temperature and oxygen concentration. Experimental oxidation data from a fine powdered graphite is plotted in Fig. 8 [29], which confirm that, indeed, effective parameters depend on temperature and oxygen concentration. The powder used by Kane et al. allowed rate information to be collected over a broad temperature and oxygen concentration range without appreciable diffusion effects. In other words, the data collected was entirely in the

kinetic regime, Regime 1 of Fig. 2, whereas with a typical porous pellet of nuclear graphite this would not be feasible.

### 3.4.3. Changing Effective Rate Constant

In Fig. 8, the effective rate constants are plotted for five different isobars of oxygen partial pressures versus temperature [29]. Careful examination shows that the effective rate constants at each temperature do not fall on top of one another. Moreover, the separation of rate constants varies as a function of temperature and the relative change in oxygen concentration. Near 800°C in Fig. 8, the effective rate constants begin to converge for the five isobars. As the temperature decreases below 800°C, the data begins to spread and the spread appears to increase with decreasing temperature although the relative change in oxygen concentration between isobars is constant. It is also worth noting that this experimental data shows lower oxygen partial pressures producing a larger effective reaction rate constant.

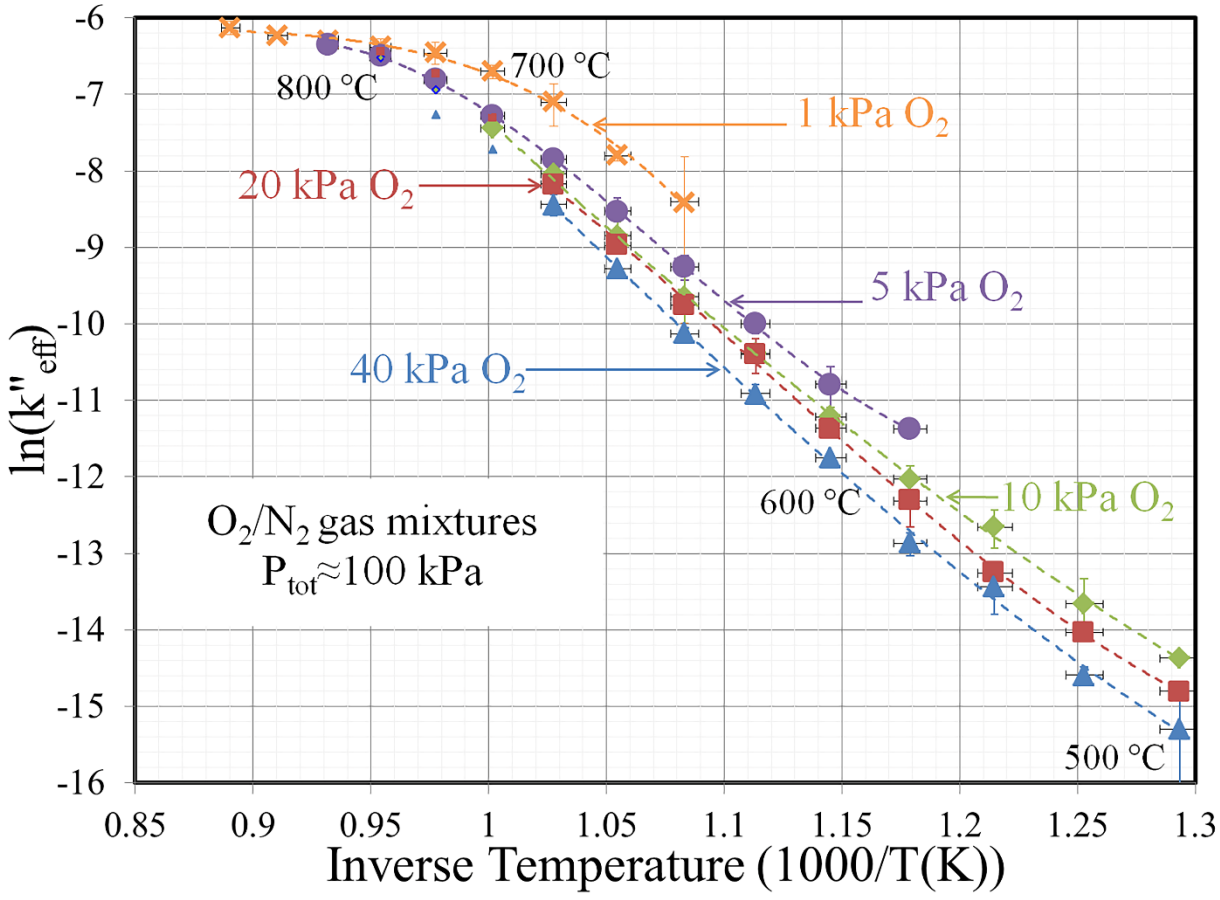


**Fig. 8.** Experimental data from Kane *et al* [29]. The effective reaction rate constant, $k''_{eff}$ is a function of temperature and oxygen concentration and has units of $^{m}/_{s}$.

Eqs. (11) and (13) are able to account for these experimental observations. The increase in effective reaction rate constant can be explained by the oxygen concentration terms in the

denominator of Eq. (13). For a given temperature, a lower oxygen concentration will decrease the magnitude of the denominator, which in turn increases the value of $k''_{eff}$. As elementary reaction rates are commonly exponentially dependent upon temperature, it is reasonable to assume that the elementary rate constants in the denominator are relatively small near 500°C and orders of magnitude greater near 800°C. For a constant oxygen concentration, the oxygen terms in the denominator will have more bearing on the effective rate constant at low temperatures because of the exponentially smaller magnitude at the lower temperatures. At high temperatures near 800°C, these same oxygen terms have little effect on the effective rate constant, and at these temperatures the oxygen term in the numerator of Eq. (11) and Eq. (12) are the only appreciable contribution of oxygen concentration to the reaction rate.

### 3.4.4. Changing Effective Activation Energy

The changing slope over the experimental range in Fig. 8 indicates that the effective activation energy changes as well. A changing effective activation energy, when the reaction is kinetically controlled, implies a change in the rate limiting elementary reaction within the fastest pathway of the reaction mechanism. If the effective reaction rate constant is assumed to have an Arrhenius temperature dependence the effective activation energy can be determined, at a constant oxygen concentration. Using the elementary rates fitted by Kane et al., Fig. 9 illustrates the changing of the effective activation energy as a function of temperature for an oxygen concentration equivalent to that in air. At low temperatures, the effective activation energy approaches 150 kJ/mol, which suggests that the desorption of $CO_2(g)$ via the indirect desorption path is nearly rate limiting (Eq. [7b]). At high temperatures, the curve begins to converge towards ~30 kJ/mol, suggesting that the dissociative chemisorption of oxygen almost entirely dictates the rate of oxidation (Eq. [4b]). Finally, near 700°C the effective activation energy peaks near 250 kJ/mol, suggesting the formation of $CO(g)$ is the predominant reaction pathway, not necessarily exclusive though, and effective rate is more or less controlled by the desorption process (Eq. [7c]) [29]. It should also be noted for comparison purposes that the effective activation energy in the temperature range of 550°C to 700°C matches relatively well with a number of nuclear graphite oxidation studies where effective activation energies range from 170–210 kJ/mol [48-59].

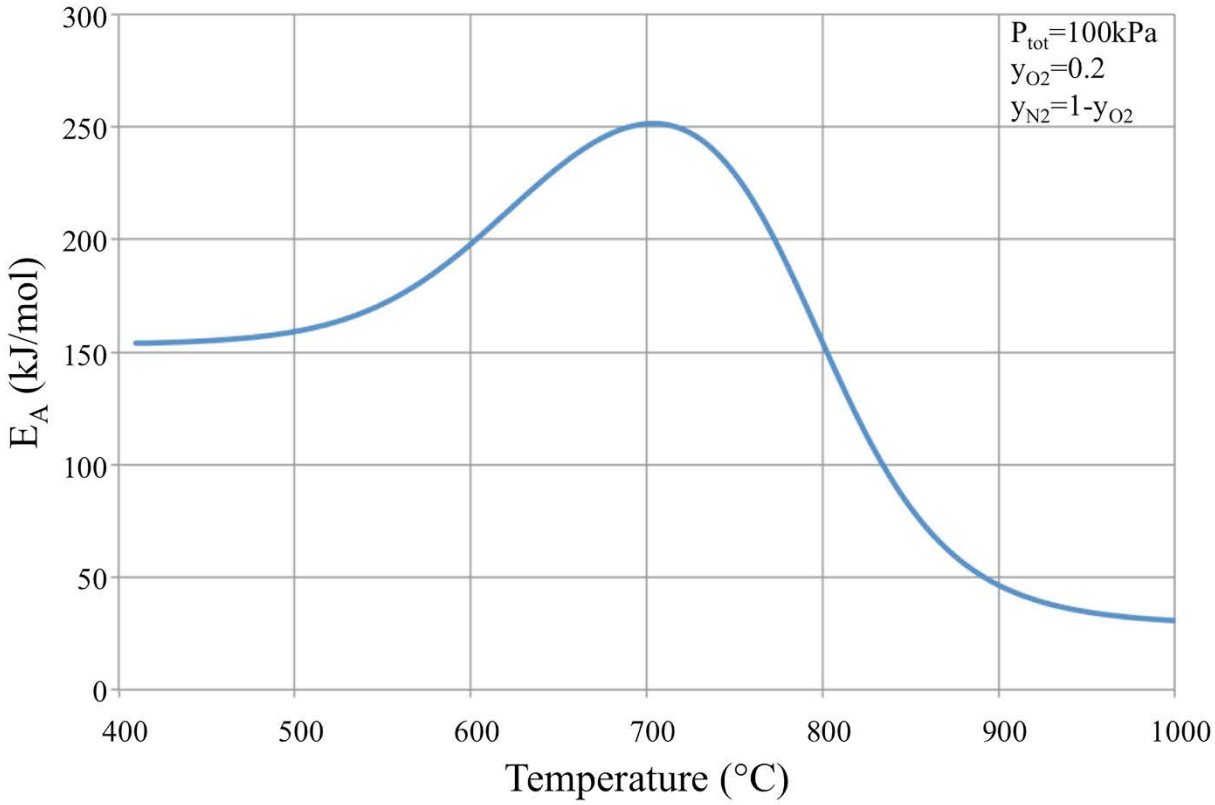


**Fig. 9.** Effective activation energy plotted as a function of temperature. The results were obtained by taking the derivative of the natural logarithm of Eq. (13). Values for the elementary reactions were taken from Kane et al. [29].

Fig. 10 shows the same data as Fig. 9, but it includes the effect of oxygen concentration on the effective activation energy. The data is falsely colored to show that oxygen concentration has on the effective activation energy over the experimental range of Fig. 8. Three trends can be observed from Fig. 10:

1. The activation energy, relative to oxygen content, is nearly constant below 550°C
2. The maximum activation energy decreases with decreasing oxygen concentration
3. In the temperature range of ~650 to 800°C, the activation energy significantly decreases as the oxygen content decreases below the nominal oxygen content of air. A temperature decrease of roughly 25°C is needed to achieve the same activation energy at 10 mol% as 20 mol%.

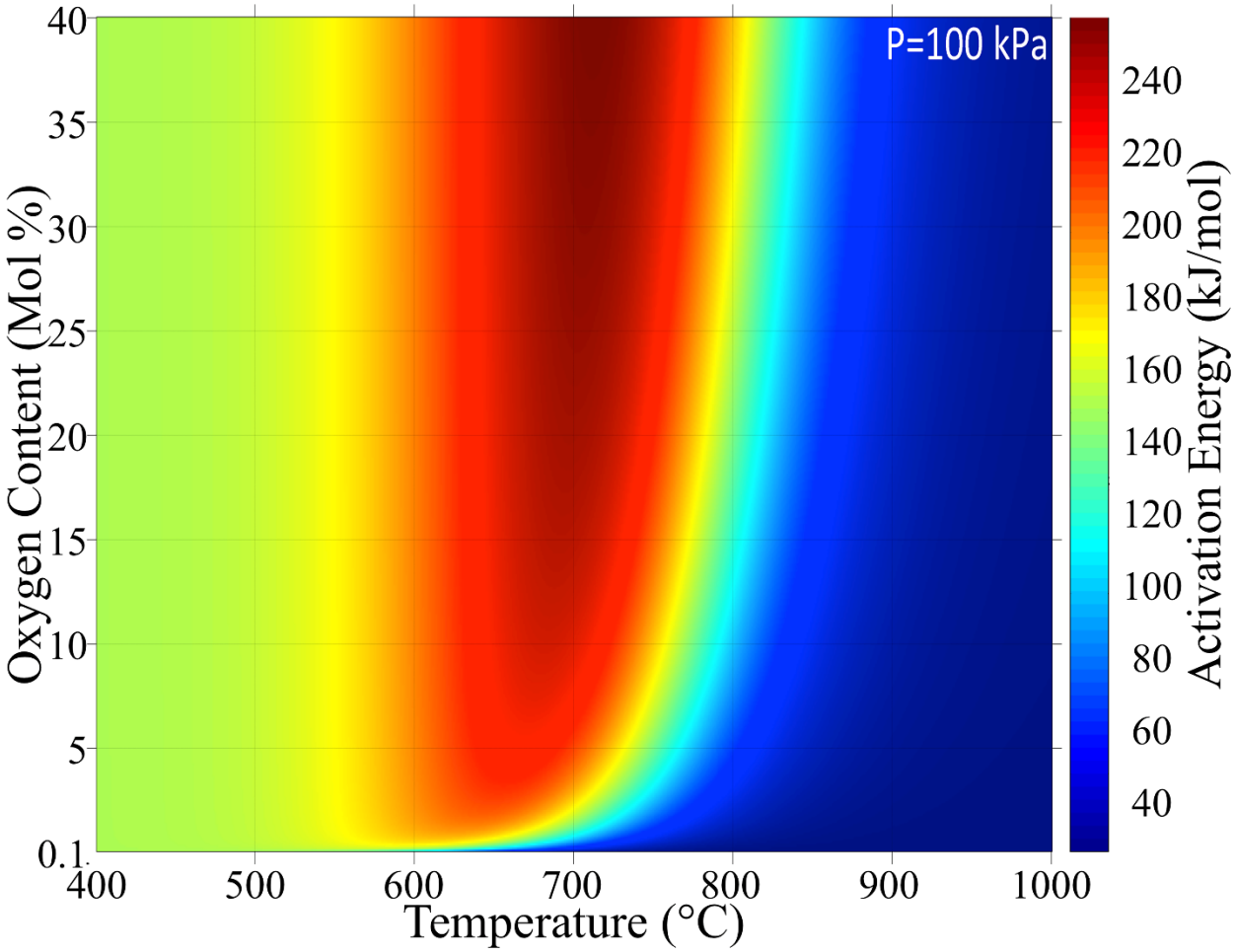


**Fig. 10.** The effective activation energy for the graphite-oxygen reaction is plotted as a function of oxygen content and temperature to show the effect of oxygen concentration on the effective activation energy.

### 3.5. Defficiencies of the Oxygen Transfer Model and an Alternative Stochastic Approach

The OTM is a deterministic kinetics model rooted in the classical chemical kinetics formalisms of basic gas-phase reaction theory. While it is well known that gas-solid reactions have additional complicating features that are not readily described by traditional chemical kinetics theory, the approach taken by Kane et al. [29] can account for many of the known influential factors in the graphite-$O_2$ reaction mechanism while still maintaining enough mathematical simplicity to obtain an explicit analytical solution. Given this simplified approach, a model such as the OTM has some deficiencies, three of which are briefly discussed here. The OTM treats all active surfaces as equally reactive, assumes each site is essentially unaffected by its local environment, and assumes that site activity does not evolve over time.

The reactivity of carbon sites is dependent upon local topology. As stated in Section 3.2, carbon atoms on the basal plane are essentially chemically inert to oxidation via $O_2$; however, defects such as grain boundaries and five- or seven- atom rings can cause local ripples and destroy the

symmetry of the perfect, ideal graphene sheet leading to these sites being susceptible to oxidation as well. The more important distinction to make in carbon site reactivity is between edge sites. As shown in Fig. 5, there are two types of edge sites in graphene and these sites have different reactivities. The so-called zigzag configuration, shown in red, has a high density of localized non-bonding π electronic states that are absent on the armchair configuration, shown in blue. The particular electronic configuration of zigzag sites plays an important role on electronic, magnetic, and chemical reactivity of zigzag graphene edges. In chemical terms, armchair edges have more aromatic stability, while zigzag edges are less aromatic and more reactive [60]. The chemical reactivity anisotropy of graphene edges has consequences on graphite reactions with $O_2$ [61-63].

While the OTM implicitly assumes no interaction between sites, the delocalized nature of electronic states in graphene and graphite make this a fairly poor assumption. In both graphite and graphene, electrons are delocalized and relatively free to move around. When a highly electronegative atom such as oxygen bonds to an edge site, the electrons in the local vicinity are held much tighter than they would otherwise. This affects electron density at neighboring sites and ultimately affects reactivity. With increasing coverage of edge sites by oxygen, the energy barrier for adsorption of oxygen has been shown to increase while for the same conditions, the energy barrier for desorption of CO and $CO_2$ decreases [25, 28, 30, 43, 45, 61, 64-69].

Finally, the OTM uses a steady-state approximation to reduce the set of differential equations describing the proposed mechanism to a set of algebraic equations. In making this assumption, the concentration of $C_b(O)$ is assumed constant. Eq. (5), which represents the surface diffusion of $C_b(O)$ along the basal plane, is inherently a time-dependent reaction step. Initially, for a pristine surface, no $C_b(O)$ will exist on the basal plane, but as oxidation proceeds, $C_b(O)$ will increase. Especially for larger crystallites having a significant lifetime in terms of oxidation, the concentration of $C_b(O)$ near the active gas-solid interface may be expected to increase appreciably over the lifetime of the crystallite. As mentioned previously in Section 3.2, $C_b(O)$ can severely affect local in plane C-C bond strength leading to a reduction in the energy barrier for desorption of reactive intermediates as CO(g) and $CO_2$(g) and effectively enhancing reactivity.

As the concentration of $C_b(O)$ builds, its effect on desorption should also vary. As a brief aside, an alternative approach to kinetics modeling, the stochastic view, merits discussion [70]. Stochastic kinetics modeling starts with the hypothesis that chemical processes occur through a chain of random events that take place with a certain probability determined by the local thermodynamic parameters. It is able to approximate the time evolution of the system as a mean trajectory of numerous individual events. While the deterministic result is a continuous, smooth, time evolution curve, the stochastic approach outlines random fluctuations around the deterministic curve.

A reasonable argument for the use of a stochastic approach in carbon oxidation is that active sites can have a distribution of adsorption and desorption energies. This is a natural consequence of the energetic heterogeneity of surface intermediates stemming from the intrinsic and induced heterogeneity of active sites in these materials [71]. For graphite as well as other carbon materials, the distribution of activation energies for $O_2$ adsorption and desorption of CO and $CO_2$ can be measured by thermodesorption experiments and often closely resembles a Gaussian distribution function [72]. The argument of surface heterogeneity is also sufficient to explain the manifestation of a fractional (and variable) reaction order for oxygen in the carbon-oxygen reaction, also known as the "persistent power law" [65].

While stochastic-based approaches can provide excellent fits of experimental data, it is important to keep in mind the nature of the fit. The experimental data represents many elementary reaction steps operating in series and parallel to produce an overall reaction. Its fitting is intended to maintain some of the typical features of a traditional kinetics model. Hurt and Calo [73] in their work on char combustion suggested the use of a semi-global mechanism comprised of several explicit reaction steps be used. While the steps may not be the true elementary reaction steps, which are likely too many and too intricately related to explicitly model, a semi-global mechanism should be able to accurately reproduce the major experimental facts while still maintaining the mathematical formalisms of classical chemical kinetics. In taking this stochastic approach, the fitted values may still retain some physical meaning.

El-Genk applied a similar methodology to oxidation of several different nuclear graphites [74-76]. In his model, he simultaneously fit both transport parameters and a semi-global kinetics model developed for films of pyrolytic carbon [67] using a non-linear multi-parameter optimization. The resulting models were applicable over a range of conditions and could even be extrapolated to some degree to modified geometries. As both transport and kinetic parameters were fitted simultaneously, there were significant variations in optimized parameters between grades. In cases such as this, caution is warranted in assigning fundamental significance to these kinetics data. Additionally, the results of such efforts remain tributary to the need to start with a large high-quality set of experimental oxidation rate data for each grade of graphite explored to fit all parameters with a high degree of certainty.

## 4. Additional Considerations for Understanding Observed Oxidation Rates

Section 3 described the graphite-oxygen reaction mechanism and layed the foundation, using the OTM as an example, for developing a single oxidation model to describe the effective reaction rate of all nuclear graphites. To implement such a kinetics model, one must be able to normalize to the reactive surface area of a nuclear graphite.

While each graphite grade has the same intrinsic rate, as shown with Fig. 2, observed oxidation rates can vary significantly from grade to grade in identical oxidation environments. Section 4 focuses on explaining these differences in terms of graphite microstructure and its evolution.

### 4.1. Microstructural Dependence of Graphite-Oxygen Reaction

Up until this point, the oxidation reaction has only been described at the atomic scale for a single, defect-free, sheet of graphene. The mechanism remains the same as the length scale increases to a single crystallite of graphite and beyond, but as discussed below, the effective rate, without proper normalization (Section 3), will be highly dependent upon the microstructure across various length scales. The structure across these length scales is in turn dependent upon the manufacturer's starting materials and processing. For a description of the general manufacturing processes for a nuclear-grade graphite, the reader is referred to the classic text edited by Nightingale [77].

Fig. 11 may be used to visualize the remaining discussion on the contribution of microstructure to the effective rate of chemical reaction. Starting at the atomic scale with a single graphene sheet (Fig. 11a), defects such as vacancies, vacancy clusters (Fig. 11b), and various other defects (Fig. 11c), increase (or modify) the ASA of the graphene sheet. Intuitively, of the two sheets shown in Fig. 11a and 11b, the defect free sheet will have a lower effective oxidation rate because there are fewer sites available for oxidation.

Moving to the nanoscale, consider the two graphite single crystals shown in Fig. 11d and e. Both contain the same number of carbon atoms at 46 per sheet, but have different shapes. As a consequence the two single crystals have different amounts of ASA. On a mass normalized basis, the single crystal in Fig. 11d has approximately $1.96\times10^{22}$ active sites per gram while the single crystal in Fig. 11e has nearly $2.31\times10^{22}$. While carbon atoms on active surface of both crystals oxidize at the same intrinsic rate, the first crystal will oxidize approximately 15% slower, initially, than the second due to the decreased number of active sites. This example illustrates the importance of a crystallite's size and shape with respect to oxidation.

For the shape of graphite single crystal, the active sites per unit mass or volume will also decrease with increasing size. In nuclear graphites, the size and shape of crystallites are highly dependent upon the precursor carbon material(s) and the graphitization schedule, which is a function of temperature and time [78].

Fig. 11f represents the mesoscale and shows the local gas-solid interface within a hypothetical open pore. At this scale, the orientation of crystallites within a nuclear graphite becomes important. As the basal plane is inert with the exception of defects, the orientation of crystallites at a pore surface can dramatically affect the ratio of ASA to TSA. At one extreme, the pore surface may have crystallites with a high density of ASA exposed such as the (110), in which case the effective density of the ASA is approximately $1.39\times10^{19}$ carbon atoms per square meter (Fig. 11g). At the other extreme, a pore may have a surface similar to the interior surface of a defect free carbon nanotube having no active sites available for oxygen chemisorption (Fig. 11h).

Progressing to the microscale, the size and shape of a pore will also affect the observed reaction rate. Assuming for simplicity pores are cylindrical, and have a surface area-to-volume ratio of $\frac{2}{r}$ (infinitly long cylinder), as the pore radius increases, all else being equal, the ASA decreases per unit pore volume. This may be an influential factor leading to the decreased oxidation performance of fine-grain graphites relative to their medium-grain counterparts assuming all other factors are equal (Fig. 3). Figs. 11i and j show small three-dimensional (3D) volumes, extracted from micro-X-ray computed tomography scans, of a medium-grain extruded graphite and a fine-grain isostatically pressed graphite, respectively. The pore fractions of these two graphites are quite similar, but the pore structure of the fine grain (Fig. 11j) visually has a larger amount of surface area per unit volume than the medium grain (Fig. 11i).

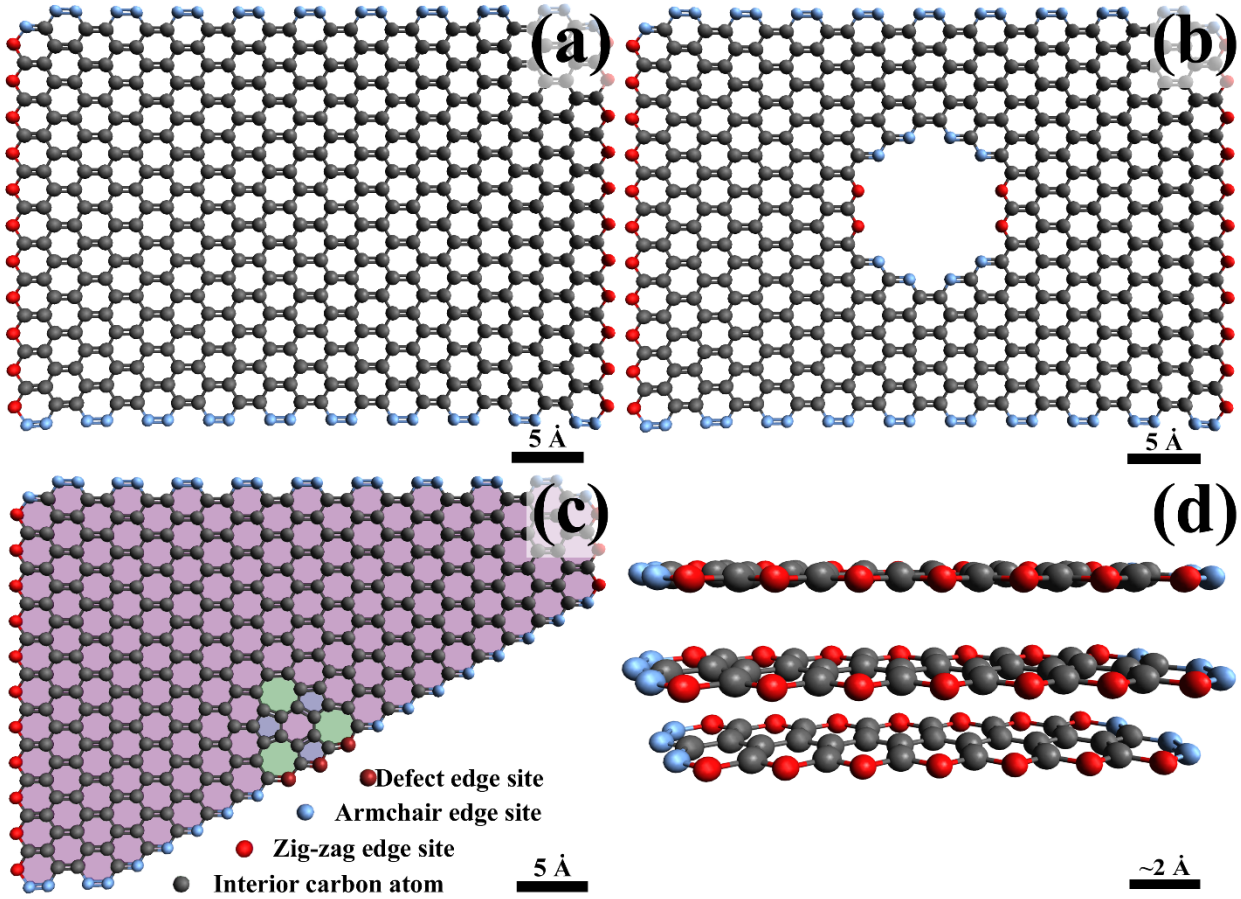

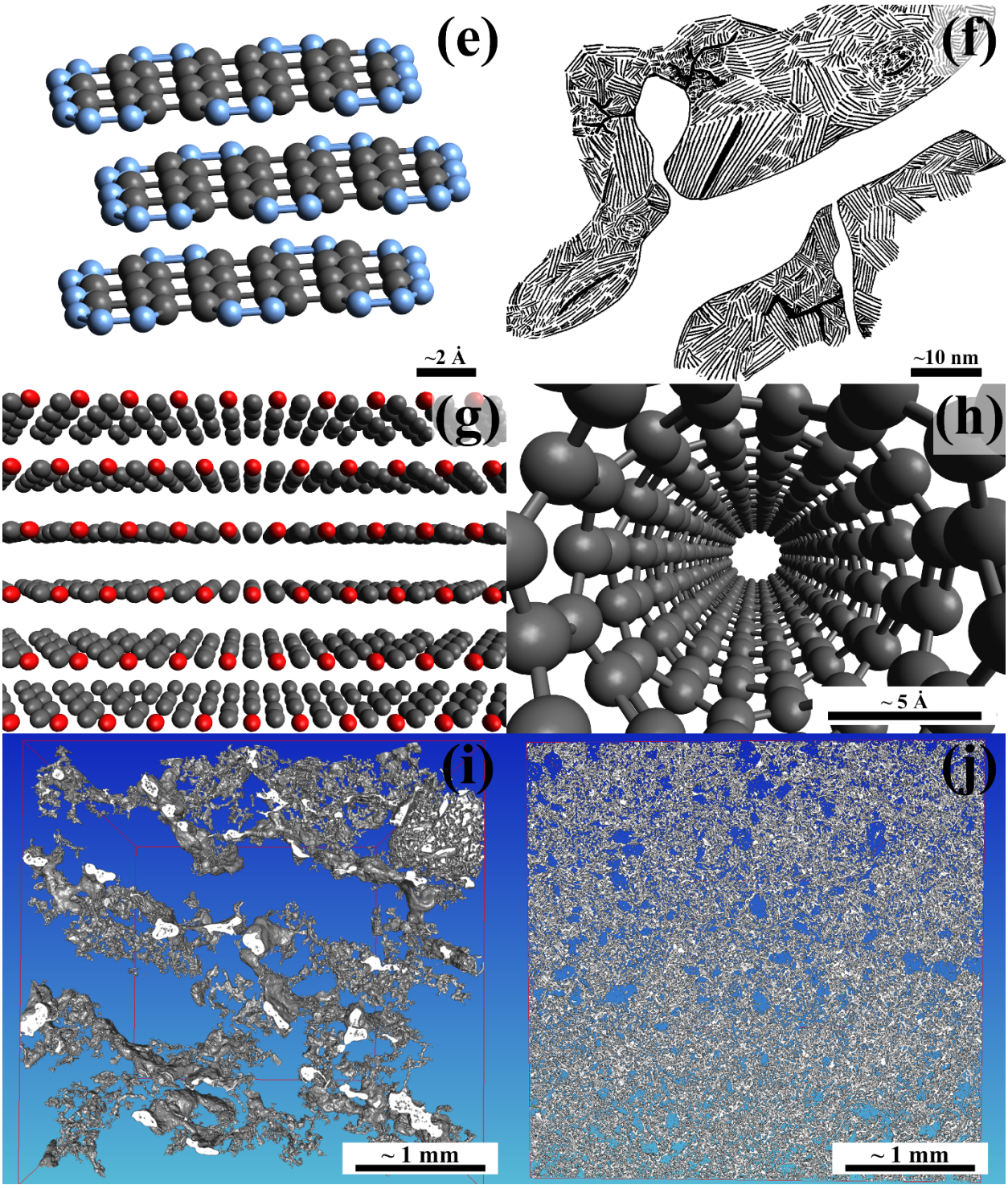


**Fig. 11.** The illustrated effects of microstructure at various length scales on the effective graphite-oxygen chemical reaction rate. For figures showing ball and stick representation of atoms, all atoms are carbon atoms. The blue carbon atoms represent carbyne-like armchair sites, the bright-red carbon atoms represent carbene-like zigzag sites. Fig. 11a shows a defect-free graphene sheet. Fig. 11b shows a similar graphene sheet to that shown in Fig. 11a. The vacancy cluster increases the number of active sites. Fig. 11c shows a complex defect composed of three

seven member rings (green) and three five member rings. This defect adds two additional carbon atoms to the sheet relative to the equivalent defect-free graphene sheet. In addition, the active sites at the edge of the defect will react at a different rate than “normal” active sites. Figs. 11d and 11e show two single crystals of graphite with the same number of carbon atoms, but different quantities of active sites. Fig. 11f is a hypothetical open pore and illustrates the local graphite-gas interface within a small section of a pore network. The line segments portray a 2-D representation of the orientation of the (001) plane of individual crystallites near the interface. Fig. 11g depicts an idealized (110) surface of a graphite crystallite. Fig. 11h shows the inert interior surface of a defect free carbon nanotube. Figs. 11i and j illustrate the pore structures of two graphite grades with similar porosities. The graphite in Fig. 11i has a significantly smaller amount of surface area than the graphite in Fig. 11j due to a greater effective pore diameter.

These factors are responsible purely for differences in the reaction rates of various graphites at low temperatures when gas transport to and from the active sites is orders of magnitude faster than the chemical reaction itself. Referring back to Fig. 2, this is represented by the extreme right of the figure, Regime 1, where the concentration of oxygen is uniform throughout the entire graphite specimen. For specimen of macroscopic dimensions, the kinetic-controlled regime only occurs over a narrow range of experimental conditions. The Thiele modulus , $\phi_n$, a parameter often used in the discussion of catalytic reactions, is one way to quantify Fig. 2 [79]. ${\phi_n}^2$ relates the ratio of surface reaction rate to an effective rate of diffusion through a porous material. As $\phi_n \to 0$, the observed reaction rate becomes increasingly controlled by the rate of chemical reaction and the observed and effective reaction rate become equal. As $\phi_n \to \infty$, the observed oxidation rate becomes increasingly limited by the effective rate of diffusion to the reactive surface. The numerical value of the Thiele modulus, assuming a first order reaction, is independent of gas concentration at the exterior surface and increases with sample size and temperature.

### 4.2. Effects of Gas Transport Through Pores on Observed Oxidation Rates

As the size of specimen studied increases to macroscopic dimensions, much more than a few millimeters in size, the range of experimental conditions over which Regime 1 of Fig. 2, $\phi_n \to 0$, becomes increasingly small. For most engineering scale tests $\phi_n$ is approximately equal to or greater than one and gas transport of reactants and products through the pore structure of a nuclear graphite must be considered to properly model the observed rate of graphite oxidation. The preliminary effect of mass transport can easily be described with the aid of Fig. 2. As temperature increases, the depth oxygen is able to penetrate (before it is consumed in the oxidation reaction) into graphite decreases. Essentially the rate of reaction increases with temperature much faster than the rate of diffusion, and at some point the reaction becomes fast enough that all the oxygen is consumed before it can fully penetrate into the entire pore structure of graphite. In this regime, the observed activation energy will be cut approximately in half as both gas diffusion, which has a relatively low activation energy, and the chemical reaction, which commonly has a significantly greater activation energy, are nearly averaged together. As

temperature increases further, the reaction rate becomes significantly greater than the rate of diffusion, $\phi_n \rightarrow \infty$ , and oxidation of the porous graphite is relegated just to the exterior surface (Regime 3, Fig. 2). In this regime, the observed activation energy decreases further to approximately 10 kJ/mol, roughly equal to the "activation energy" for gaseous diffusion. The Thiele modulus provides a convenient approach for the description of porous gas-solid reaction systems and is thoroughly described in many elementary transport, chemical reaction engineering, and catalysis texts [8, 9, 79-85].

Although the effect of gas transport on graphite oxidation is fairly well understood on a qualitative level, there are additional subtle yet appreciable effects that are often ignored or overlooked in the nuclear graphite literature. The first is the assumptions made regarding Fick's first law. Fick's law for a binary system composed of Gases A and B may be written as

$$N_A = -[C_T]D_{AB}\nabla y_A + y_A(N_A + N_B) \tag{14}$$

where the molar fluxes, $N_A$ and $N_B$, are relative to a fixed point. This form has only minor restrictions as it assumes only a fixed total gas concentration, an invarient diffusivity with respect to gas composition, and the components are adequately decribed by an ideal gas equation of state. The second term on the right-hand side expresses the net "drift" velocity of the system when there is a net transport of molecules in one direction. The simpler and more commonly used form of Fick's first law is

$$N_A = -[C_T]D_{AB}\nabla y_A \tag{15}$$

which is the same as Eq. (14) with the exception of the "drift" velocity term. Eq. (15) is nearly valid under two conditions: the first is equimolar counter-diffusion, where

$$N_A + N_B = 0 \tag{16}$$

Eq. (16) is approximately valid when the concentration profiles across a system of Species A and B are symmetric and the two species are very similar in size, as in molecular weight, and functionality (for instance both species being small non-polar molecules). The second case where Eq. (15) holds is a dilute solution scenario as $y_A \rightarrow 0$. When $y_A$is small, $y_A(N_A + N_B)$ becomes negligible relative to the concentration driven transport. With the exception of chronic oxidation due to minor impurities in the HTGR inert coolant gas, neither case is likely applicable for air ingress scenarios.

When gas transport contributes significantly to the observed oxidation rate, it is also important to account for mass transfer through the boundary layer seperating the bulk gas and exterior graphite surface. This is normally done through the use of empirical mass transfer correlations. A majority of mass transfer correlations are derived from analogous heat transfer correlations where it is often implicitly assumed that there is no net flow across the boundary layer. In a reaction system such as the graphite-oxygen reaction, this assumption simply is not valid under

most relevant oxidation scenarios and the appreciable flow of mass across the boundary layer will retard mass and heat transfer by modifying the thickness of the boundary layer. When there is a net flow from a gas-solid interface towards a solid, mass and heat transfer are enhanced as the effective thickness of the respective boundary layers are decreased. When there is a net flow in the opposite direction, toward the gas phase, the effective thickness of the boundary layer increases and mass and heat transfer across the boundary layer correspondingly decreases [86-91].

Considering Eq. (3) is helpful in the following discussion. When $CO_2(g)$ is the dominant reaction product, there is one mole of $CO_2(g)$ produced for every mole of $O_2(g)$ consumed. Once the system has reached a pseudo-steady state, there is no net molar flux across the boundary layer. Once the amount of $CO(g)$ becomes appreciable, this is no longer the case. Even by relatively conservative measurements by 650°C, approximately 33% of the reaction product is $CO(g)$. By 700°C many estimate the percentage to be closer to 60% [29, 51, 92, 93]. Regardless of the actual fraction, only one molecule of $O_2(g)$ is consumed for every two molecules of $CO(g)$ produced causing a significant decrease in mass and heat transfer due to a net molar flow of gas from the gas-solid interface into the bulk gas stream.

This effect has been noted in the nuclear graphite literature [94]. El-Genk et al. empirically determined a mass transfer correlation for the observed decrease in mass transfer from that of traditional correlations, but did not correlate the difference to a net flow directed outwards from the graphite exterior surface [94]. It is important to realize that the ratio of $CO(g)$ to $CO_2(g)$ produced during oxidation will significantly impact boundary layer thickness and as a consequence the rate of mass or heat transport across the boundary layer. Thus, correlations such as these based on limited experimental observations of nuclear graphite may not hold over the entire range of interest.

Finally, when mass transport plays an appreciable role in the observed rate of oxidation, the presence of $CO(g)$ and $CO_2(g)$ increases the probability of homogeneous gas phase reactions and additional heterogeneous gas-solid reactions. Two potential reactions of interest are:

$$CO(g) + O_2(g) \rightarrow CO_2(g) \tag{17}$$

$$C_eO + CO(g) \leftrightarrow CO_2(g) + C_e \tag{18}$$

The homogeneous gas phase reaction, Eq. (17), will reduce the local concentration of oxygen within a pore which may retard the local effective reaction rate at a surface. At the same time, Eq. (17) is an exothermic reaction and could cause local heating of the gas phase. This reaction is not expected to play a major role in the observed rate of reaction unless small amounts of moisture and/or hydrogen are present. Hydrogen and moisture are known to catalyze this gas phase reaction [95-97]. The chemistry of the interaction of hydrogen in carbon monoxide

oxidation is well established and kinetic models should be capable of predicting the rate of $\mathrm{CO(g)}$ oxidation over a large range of conditions [98].

Eq. (18), shown above as a reversible gas-solid reaction, is in many ways identical to Eq. (17) other than it occurs at the gas-solid interface rather than in the gas phase. As illustrated in Fig. 12, a $\mathrm{CO(g)}$ molecule forms a bond with two adjacent $C_eO$ surface intermediates (Fig. 12 a and b). This effectively weakens the bonds between the adjacent $C_e$ atoms and their bonded atomic oxygen. From this state, one of the $C_eO$ bonds may weaken and simultaneously form a stonger bond with the adsorbed carbon from the $\mathrm{CO(g)}$. When this occurs, the carbon atom may desorb from the gas-solid interface as $\mathrm{CO_2(g)}$ (Fig. 12 c and d). Experimental work has shown measurable differences in the rate of chemical reaction between graphite and oxygen when small quantities of $\mathrm{CO(g)}$ are added to the reactant gas mixture [99].

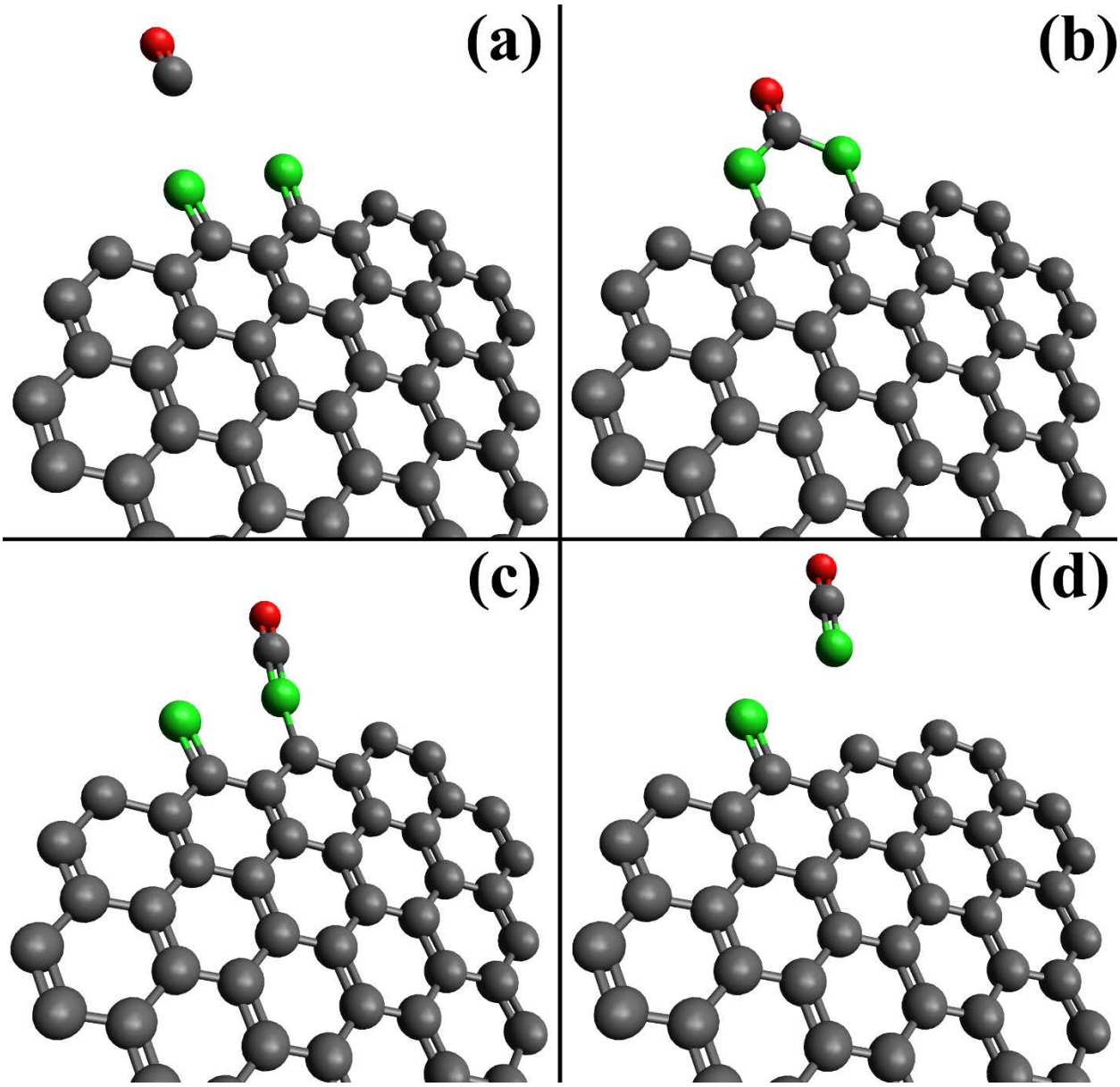


**Fig. 12.** An illustration of one possible interaction between $CO(g)$ and semiquinone reactive intermediates to form $CO_2(g)$. The gray atoms represent carbon atoms, green atoms represent oxygen originally attached to the graphene sheet as a semiquinone reactive intermediate, and the single red atom represents oxygen from the carbon monoxide gas molecule in Fig. 12a.

### 4.3. Effects of Dynamic Pore Evolution on Effective and Observed Rates

Although it has not been explicitly stated so far, it should be obvious from Sections 4.1 and 4.2, that the initial pore structure of nuclear graphite significantly influences both the effective and observed rate of reaction. However, the pore structure is not static. The oxidation of graphite produces only gaseous reaction products, and consequently the pore structure is dynamically changing over the entirety of its exposure to oxygen at elevated temperatures. This dynamic

evolution will affect both the effective and observed rates of chemical reaction. It is well known that nuclear graphites possess both open and closed porosity. What happens as the open porosity grows and previously closed porosity becomes exposed?

3D μX-ray computed tomography is an excellent method for interrogating the macropore [100] structure of nuclear graphites non-destructively. In the text below, macroporosity segmented from two different μX-ray computed tomography data sets, will be used to semi-quantitatively illustrate the effects of pore evolution. The effect of oxidation is artificially simulated by isotropically dilating existing macropores incrementally though the use of a number of image analysis techniques.

Fig. 13 shows a single binary slice from a large 3D volume reconstructed from tomographic projections of a medium grain extruded nuclear graphite. The open porosity in the volume is repeatedly dilated incrementally by 1 pixel length to artificially simulate an isotropic oxidation of the graphite pores. Note that the optical micrograph in Fig. 13j is a cross section of an oxidized medium-grain vibrationally molded graphite and shows similar results to the binary images at higher levels of conversion, $\alpha$. Fig. 13 visually demonstrates three important trends in the evolution of the pore structure with increasing levels of oxidation. First, the total surface area changes as pore structure evolves.

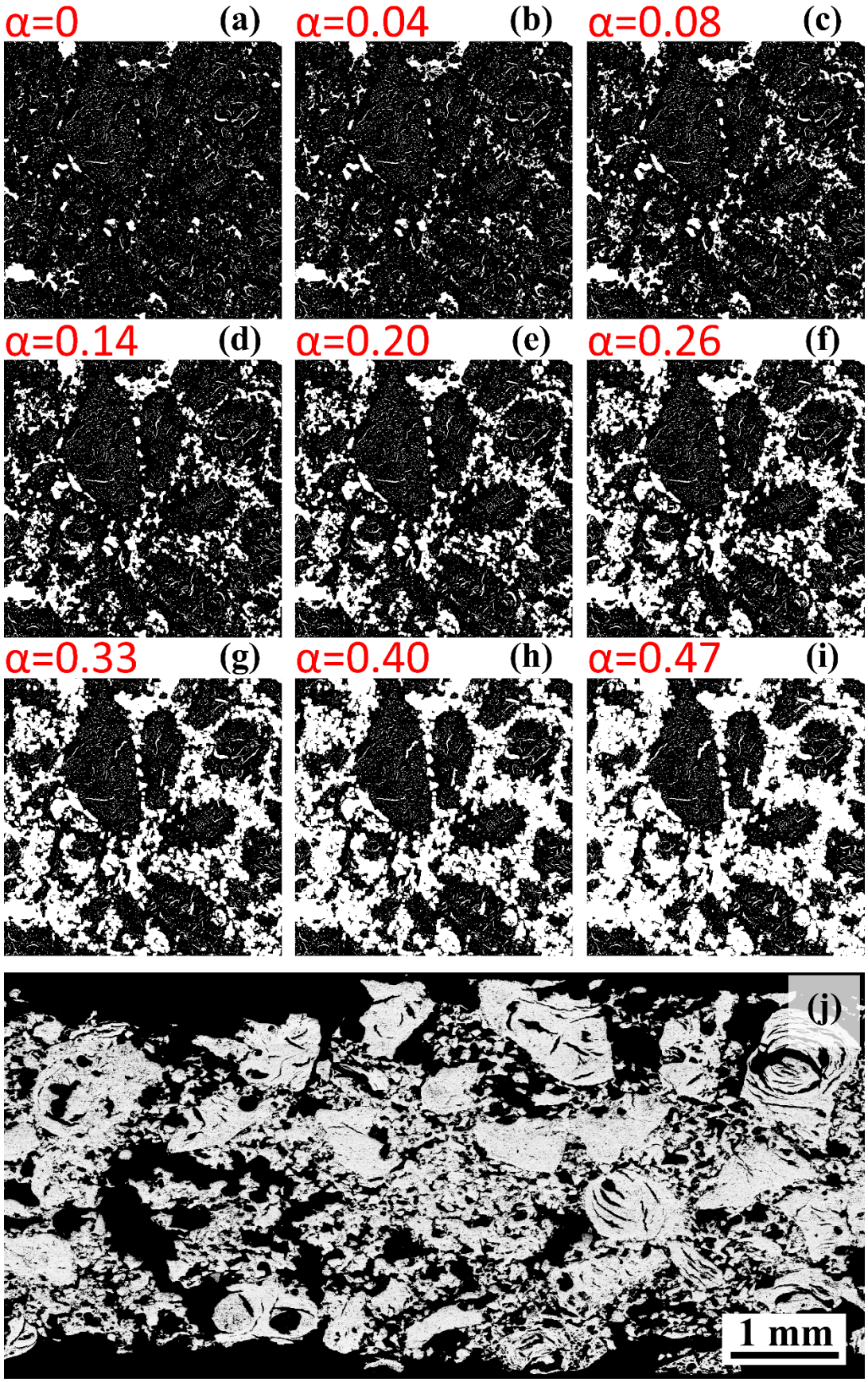
α=0
(a)
α=0.04
(b)
α=0.08
(c)
α=0.14
(d)
α=0.20
(e)
α=0.26
(f)
α=0.33
(g)
α=0.40
(h)
α=0.47
(i)
(j)
1 mm

**Fig. 13.** The left side with labels $\alpha = 0$ to $\alpha = 0.47$ show a simulation of pore structure evolution in graphite. The images are binary representations of a single slice of a 3-D X-ray tomographic reconstruction with an initial pixel resolution of approximately 4 μm. The volume was isotropically eroded to approximate pore structure evolution during oxidation at low temperatures. The gray-scale micrograph on the right is a stitched mosaic of optical images from a medium-grain vibrationally molded graphite oxidized at 600°C to approximately 36% mass loss. Oxidation took place in a calibrated gas mixture with a nominal composition of 21% oxygen and a balance of nitrogen. The approximate gas velocity of the sample surface was approximately 0.5 cm/s at standard temperature and pressure.

To illustrate the changes in total surface area as oxidation increases, Fig. 14 shows the calculated total surface area of artificial dilations relative to the initial surface area estimated from observable macropores via μX-ray CT. An initial increase in surface area up to approximately 40% oxidation is observed, after which the surface area begins to decline. This phenomenon has been observed experimentally by Fuller and Okoh using nuclear-grade graphite [55]. Assuming a constant ratio of ASA to TSA, the oxidation rate per unit volume would locally mirror the change in TSA. The rise in surface area is likely caused by the opening of previously closed porosity. From numerical isotropic dilations of pore stuctures, the surface area peaks between 30% and 40% oxidation depending on graphite grade and gradually decreases toward its initial value as the pores increase in size and interconnectivity.

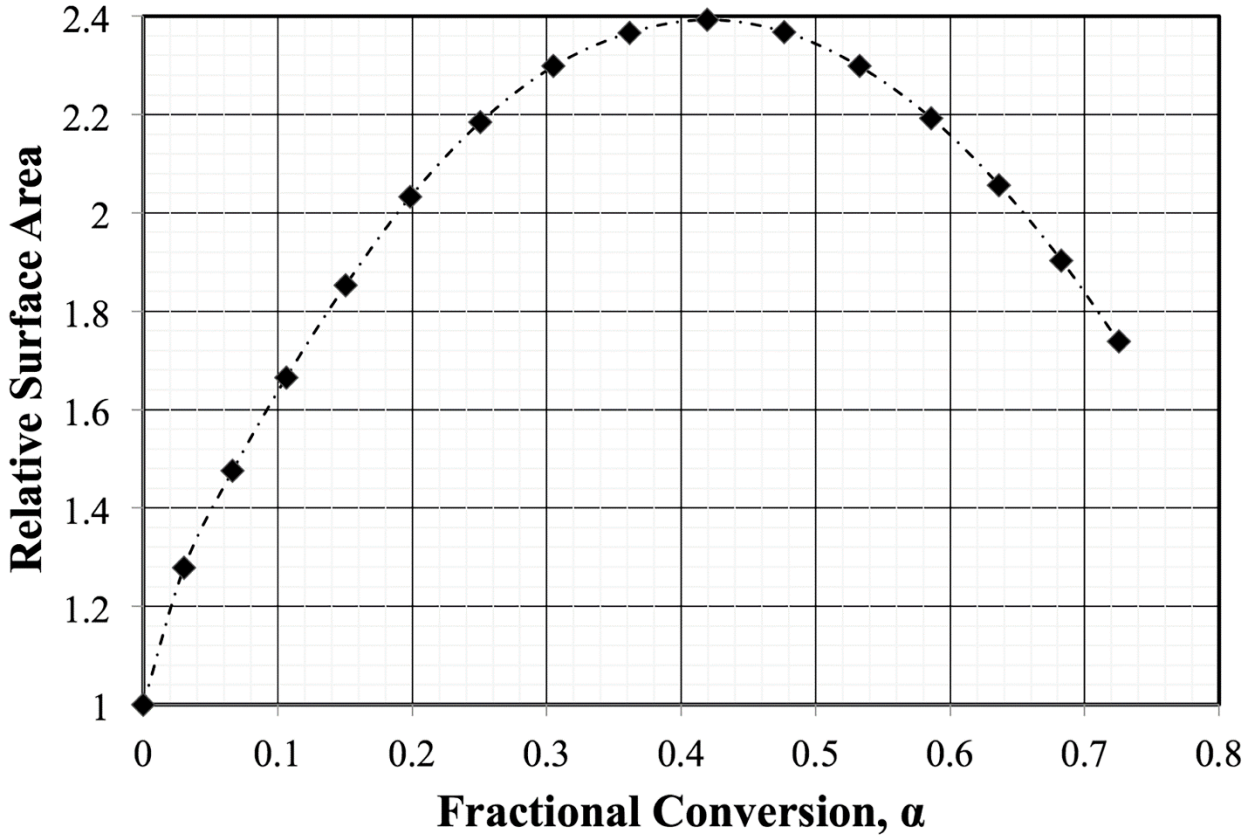


**Fig. 14.** The effect of the artificial isotropic oxidation of an extruded graphite on the total surface area within open pores. The surface area estimates are normalized to the surface area at a conversion level of 0. This figure was created for illustration purposes only and should not be used quantitatively. The tomographic reconstuction does not account for all porosity, only macropores [100] within the resolution of the tomographic scan.

Second, as the pore structure evolves, the effective rate of gas diffusion through the pore structure will inevitably change as well. Fig. 15 shows estimates of the effective diffusion coefficent for a binary gas mixture through the macropores of the tomographic reconstruction. The plot in Fig. 15 is normalized to the bulk diffusion coefficient for the gas pair. As pores become larger and the interconnectivity increases, the effective rate of transport through the porous material should increase. This is in part due to the increased cross-sectional area available for gasses to travel, but also due to a decrease in geodesic path length as pores grow. In the case of the artificial isotropic oxidation, the increase in the diffusion coefficient is approximately linear with respect to conversion.

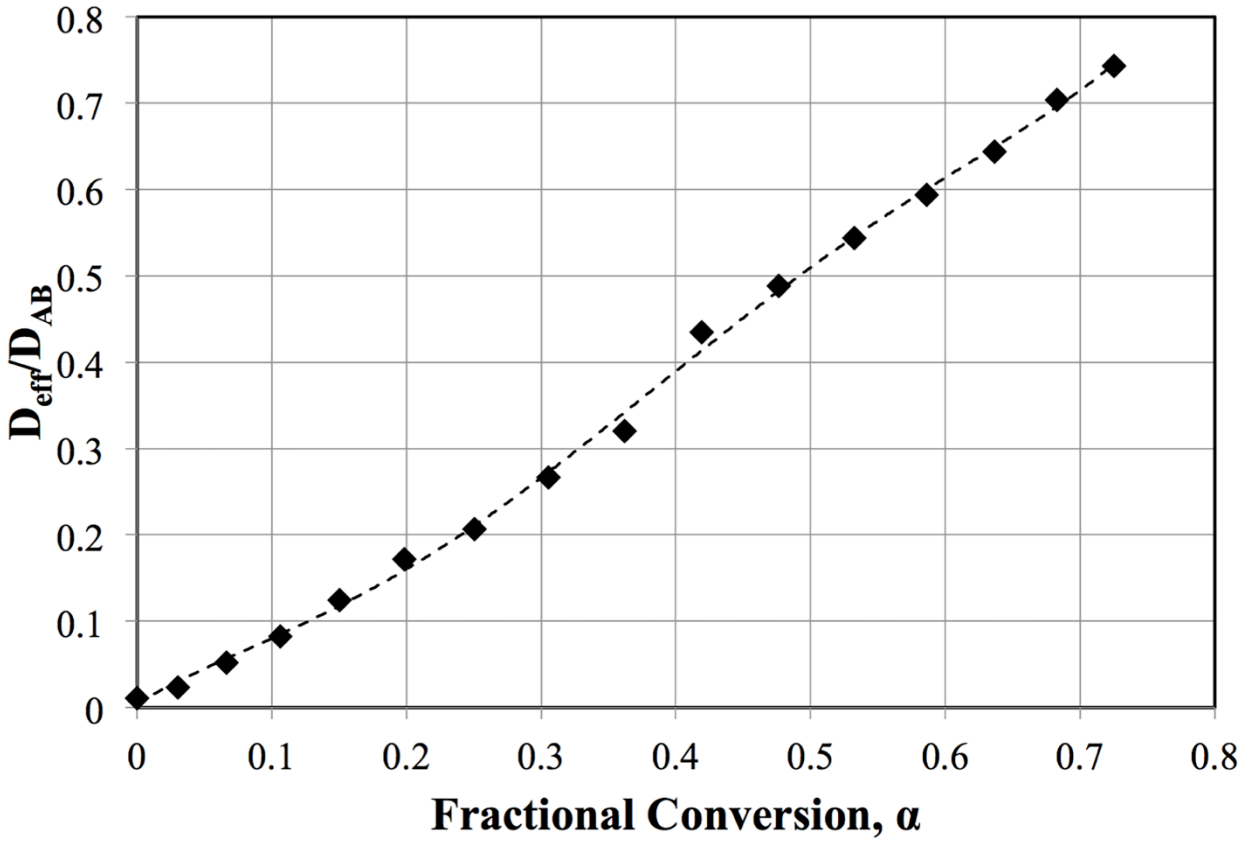


**Fig. 15.** The effect of the artificial isotropic oxidation of an extruded graphite on the effective diffusion coefficient of a gas mixture. The effective diffusion estimates are normalized to the bulk diffusion coefficient for the same gas mixture. This figure was created for illustration purposes only and should not be used quantitatively. The tomographic reconstuction does not account for all porosity, only large macropores [100].

Finally, examination of Figs. 13e–i shows that large particle-like regions are left nearly "untouched" by oxidation. The similarity of these regions to the filler particles in Fig. 13j suggests that these regions are large filler particles. The binder-matrix contains a majority of the macroscopic porosity for gas transport, and at higher levels of conversion, the binder around a particular filler particle may completely oxidize well before the filler particle itself is substantially affected. At these higher levels of conversion, filler particles may become dislodged from the bulk material effectively enhancing the observed rate of mass loss to a bulk component.

## 5. Predicting Observed Rates via Intrinsic Kinetics and Microstructural Parameters

Sections 3 and 4 provided an overview of the reaction mechanism, microstructure effects, and other phenomena that dictate both the effective chemical reaction rate and the observed oxidation rate for high purity, porous graphites. Section 5 takes the qualitative descriptions in sections 3 and 4 and incorporates them into a single model applicable to any graphite material that meets

the three basic assumptions outlined in Section 3.1. Using an intrinsic oxidation model, for example the OTM described in Section 3.4, allows all nuclear graphite grades to be descibed using a single chemical reaction rate. This allows the differences in the observed oxidation rates between grades to be described purely by structural parameters unique to each grade. These structural parameters in turn have physical meaning and can therefore be measured for a specific graphite grade.

### 5.1. Equations for describing the observed oxidation rate

Eqs. (19–30) make up the generalized system of equations needed to fully predict the observed rate of oxidation for any nuclear graphite. The meaning of each variable and its SI equivalent units are described in the nomenclature section. The structurally dependent variables, unique to each grade, are bolded and given a different font color to distinguish them from the remaining variables and constants affecting the observed oxidation rate. The highlighted structural terms will be discussed in more detail in Section 5.2. In an attempt to promote an easier understanding of the meaning and arguments of Eqs. (19-30), the discussion below will be put in terms of Fig. 2.

$$\frac{\partial \rho}{\partial t} = -\left(\frac{\partial [CO]}{\partial t} + \frac{\partial [CO_2]}{\partial t}\right) = k_{eff}^{"} \boldsymbol{S_A} [O_2] \tag{19}$$

$$\boldsymbol{N_i} \cong -[C_T] \boldsymbol{D_{eff_{iM}}} \nabla y_i + y_i (\boldsymbol{N_i} + \boldsymbol{N_M}) \tag{20}$$

$$\frac{\partial \varepsilon [O_2]}{\partial t} = -\nabla \boldsymbol{N_{O_2}} + \left(1 - \frac{1}{2} x\right) k_{eff}^{"} \boldsymbol{S_A} [O_2] \tag{21}$$

$$\frac{\partial \varepsilon [CO]}{\partial t} = -\nabla \boldsymbol{N_{CO}} + x k_{eff}^{"} \boldsymbol{S_A} [O_2] \tag{22}$$

$$\frac{\partial \varepsilon [CO_2]}{\partial t} = -\nabla \boldsymbol{N_{CO_2}} + (1 - x) k_{eff}^{"} \boldsymbol{S_A} [O_2] \tag{23}$$

$$\frac{\partial \varepsilon [I]}{\partial t} = -\nabla \boldsymbol{N_I} \tag{24}$$

$$\frac{\partial (\rho c_p T)}{\partial t} = \nabla \cdot (\boldsymbol{k_T} \nabla T) + k_{eff}^{"} \boldsymbol{S_A} [O_2] \Delta H_{rxn}(x) \tag{25}$$

The extreme right side of Fig. 2 represents the ideal state where the rate of chemical reaction is orders of magnitude slower (infinitely slower) than the rates of mass and heat transport. Equivalently, the Thiele modulus approaches 0, $\phi_n \to 0$. Under these conditions gas species flow through the pore structure so fast that the concentration of oxygen throughout the entire pore space of a sample is constant and is also equal to the oxygen concentration of the bulk gas ($C_{Max}$ in Fig. 2). In this case, Eq. (19), the effective reaction rate is the only important equation in understanding the rate of oxidation. The time and spatial gradients with respect to concentration and temperature make Eqs. (20-25) nearly $0 = 0$. It is worth noting here that if and only if these

conditions hold the effective chemical reaction rate is equal to the observed chemical reaction rate.

As highlighted in section 4, the ASA is expected to change over time as the pore structure continues to evolve within graphite and $\boldsymbol{S_A}$ describes this change. $\boldsymbol{S_A}$ is dependent upon each graphite grades initial structure and consequently on its changing state over time.

Returning to Fig. 2, keeping in mind that the effective reaction rate has an exponential temperature dependence and gas diffusion $\sim T^{3/2}$ dependence, as temperature increases, the rates of chemical reaction, Eq. (19), and mass diffusion, Eq. (20), quickly become similar in magnitude. This is qualitatively described by Regime 2 in Fig. 2, or quantitatively by a Thiele modulus on the order of 1. As the effective reaction rate becomes appreciable relative to mass transfer, the concentration of oxygen is no longer constant througout a graphite specimen, but rather decreases with increasing depth into the specimen. In Regime 2, Eqs. (21-24) become critical in determining the concentration of oxygen and other species as a function of location within graphite. Analogously, as the rate of heat generation from the exothermic chemical reaction approaches the rate of heat removal from graphite, Eq (25), the energy conservation equation, becomes important in predicting the temperature as a function of spatial position within graphite.

In Regime 2, a gradient in oxygen concentration and/or temperature causes the effective reaction rate, Eq. (19), to vary spatially. Eq. (19) no longer equates directly to the observed oxidation rate. Instead, integration of Eq. (19) over all sample space is needed to determine the observed oxidation rate. The observed oxidation rate is represented by Eq. (26). Similarly, the overall conversion, or normalized total mass loss, Eq. (27), can be determined by integrating Eq. (19) over all space and all time. The overall conversion can be used to provide a direct comparison of experimental mass loss data and simulation results. Ultimately, in order to model the change in physical, thermal, and mechanical properties as a function of oxidation, the extent of local oxidation damage must also be known. Eq. (28) describes the local conversion of graphite along an arbitrary spatial axis, $z$.

$$r_{Obs} = \int \frac{\partial \rho}{\partial t} dV \tag{26}$$

$$\alpha = \int \int \frac{\partial \rho}{\partial t} dt\, dV \Big/ \int \rho_0\, dV \tag{27}$$

$$\alpha(z) = \int \frac{\partial \rho(z)}{\partial t} dt / \rho_0(z) + \alpha_0(z) \tag{28}$$

The final equations needed to completely describe graphite oxidation are the bounding conditions for temperature and each gas species. The boundary conditions may take a variety of forms depending on the needs and complexity of a model. Here, the boundary conditions as written in Eqs. (29) and (30) describe how mass and or heat is transferred across the boundary

layer between a bulk gas and sample surface. Although these conditions may begin to have an appreciable effect in Regime 2, the biggest impact may be observed as graphite oxidation transitions to Regime 3 (Fig. 2). In Regime 3, $\phi_n \gg 1$, gas transport is significantly slower than the rate of chemical reaction and thus the transport of oxygen through the boundary layer to the sample surface becomes the rate limiting process. These boundary conditions are typical Robin type boundary conditions with the exception of $\theta_y$ and $\theta_T$. As discussed briefly in Section 4.2, at higher temperatures where mass and heat transfer across a boundary layer become important, the major reaction product is $\mathrm{CO(g)}$. This causes a net molar flow of gas through the boundary layer towards the bulk gas and will substantially decrease the rate of mass and heat transfer across the boundary layer (compared to an equimolar counter diffusion condition Eq. 16).

$$\left(-[C_T]\boldsymbol{D_{Eff_{iM}}}\nabla y_i\right)\Big|_{GS\ Interface} \cong k_{x,loc}\theta_y \Delta y_i \tag{29}$$

$$\left(-\boldsymbol{k_T}\nabla T\right)\Big|_{GS\ Interface} \cong h_{x,loc}\theta_T \Delta T \tag{30}$$

### 5.2. Structurally Dependent Oxidation Parameters

As mentioned above, the highlighted terms are used to distinguish parameters effected by a graphite's structure and its evolution with time. The effects of structure on the observed rate of oxidation are distilled here into three simple terms: $\boldsymbol{S_A}$, $\boldsymbol{D_{eff_{iM}}}$, and $\boldsymbol{k_T}$.

$\boldsymbol{S_A}$ is effectively an average ASA per-unit volume and is unique to each grade of nuclear graphite. As described in Section 4.1, the absolute rate of the chemical reaction is highly dependent upon the amount of ASA that exists within the open pore structure of graphite. $\boldsymbol{S_A}$ is dependent upon factors such as the size and arrangement of crystallites at the gas-solid interface of pores (and sample exterior) as well as the size and morphology of the grade's pore structure. Given the pore structure will evolve over time, Section 4.3, $\boldsymbol{S_A}$ will be dependent on the local conversion as well. In the extreme case that the observed oxidation rate is purely rate-limited by the gas-solid reaction, $\boldsymbol{S_A}$ is the only microstructural factor affecting the oxidation. It is the authors' unanimous opinion that $\boldsymbol{S_A}$ is the largest contributor to the large variation in the observed rates of various graphite grades under identical conditions (Fig. 3).

$\boldsymbol{D_{eff_{iM}}}$, the effective diffusion coefficient, is purely a function of the pore structure for the graphite of interest. Porous diffusion is often classically described by a relation similar to

$$\boldsymbol{D_{eff_{iM}}} = D_{iM}\boldsymbol{f_p} \tag{31}$$

where $D_{iM}$ is the diffusivity of the gas mixture and $\boldsymbol{f_p}$ is a porous structural factor. The advantage of this description is $\boldsymbol{f_p}$ is the only factor dependent upon the pore structure. An equivalent factor can be used to describe Knudsen diffusion through pores where the mean free path of a gas molecule is on the order of the pore diameter. Knudsen diffusion likely plays a measurable role in the effective rate of diffusion through a particular graphite as porosimetry

measurements show an appreciable fraction of porosity in the mesopore range [100-102]. $f_p$ has taken a variety of forms in literature, but here it is shown with three different contributions related by Eq. (31).

$$f_p = \frac{\varepsilon\sigma}{\tau^2} \tag{32}$$

ε, the local open porosity, accounts for the restriction of transport to the pore structure rather than the entire cross-sectional area of the graphite (Fig. 16a). $\tau$, tortuosity, accounts for an increase in gas transport distance relative to the system dimensions. Tortuosity, as shown in Eq. (31), is a ratio of geodesic to Euclidean distance (Fig. 16b). Tortuosity factors often appears in catalysis and porous diffusion literature simply as a correction factor to allign $D_{iM}$ with experimental measurements of $D_{eff_{iM}}$. Several references suggest the squared term in the denominator of Eq. (31) is physically more meaningful [79, 83, 91, 103]. Finally, σ, termed a constriction factor, accounts for decreases in the rate of mass transfer due to periodic expansions and contractions within pores, which ultimately causes the local flux vector within a pore to deviate from the pores center line (Fig. 16b) [79, 104, 105] .

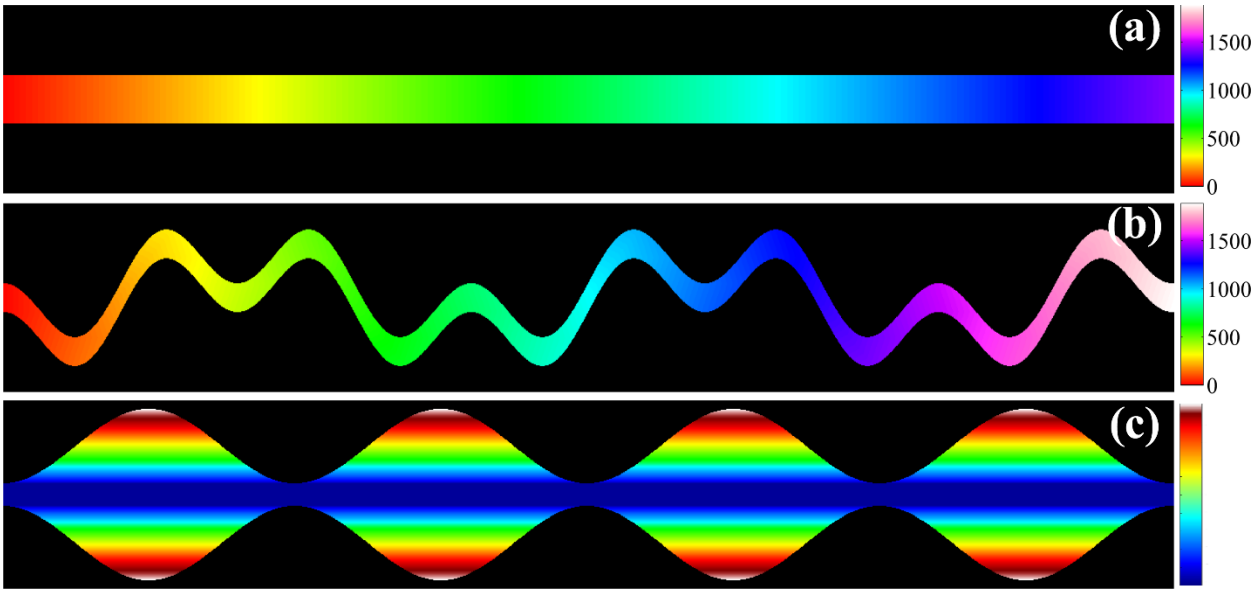


**Fig. 16.** An illustration of three different pores (pathways) that traverse the same distance through a material. These pores are idealized illustrations of the effects of ε, σ, and $\tau$ on the effective gaseous diffusion coefficient through a pore structure. Fig. 16a illustrates the effect of ε. Fig. 16b illustrates the effect of $\tau$. Fig. 16c illustrates the effect of σ. The false color maps in Fig. 16a and 16b are shown in the same arbitrary distance units to illustrate the increased path length in Fig. 16b relative to 16a. The false color map in Fig. 16c illustrates distance from the unrestricted centerline path of the pore.

The final structural factor, $k_T$, is the effective thermal conductivity. $k_T$ will vary for each grade due to differences in size, shape, and texturing of crystallites within the filler and binder and by

the types and quantities of line and point defects within the crystallites. This is reflected in Eq. (32) by the $k_g$ term.

$$k_T = k_g f_G \tag{33}$$

The effect of porosity on thermal conductivity is in some sense analogous to the effect of porosity on $D_{eff_{iM}}$ and is denoted by $f_G$ in Eq. (33).

$$f_G \sim \propto \frac{(1-\varepsilon)\sigma_G}{{\tau_G}^2} \tag{34}$$

$1-\varepsilon$ represents the fraction of the total sample volume occupied by graphite and $\sigma_G$ and $\tau_G$ have similar meaning to the corresponding values in Eq. (31). With respect to heat transport, conduction through the graphite may not be the only contributing factor. Conduction and possibly natural convection in the gas phase as well as radiant heat transfer may play small, but measurable roles in the overall rate of heat transfer within the graphite. This is noted in Eq. (33) by the use of proportionality, rather than an equality sign.

### 5.3. Advantages of a Microstructurally Dependent Oxidation Model

A graphite's microstructure is inherently tied to its properties and ultimately its performance in a nuclear reactor. Therefore the key driver for graphite oxidation research in a hypothetical accident scenario is not the determination of the rate of reaction under a given set of conditions, but rather the induced change to the microstructure inflicted by oxidation.

As stated in Section 2 current kinetics models must be coupled with mass transport (at a minimum) in order to:

1. predict how far oxidation damage will penetrate into a specimen.
2. describe the changing microstructure as oxidation progresses.

A number of models have been developed in order to better address these issues [49,76,106-109]. Each one of these models significantly improves the prediction of mass loss under a given set of conditions. The limitations of these models result from their dependence upon observed reaction rate data taken from bulk nuclear graphite specimen. As noted specifically in Fig. 3, "pure" kinetics data can only be achieved in Regime 1, which can only be obtained in a very narrow temperature range. Thus, the kinetics data used is inevitably already influenced by gas transport (Regime 2), the very process these models attempt to account for. Additionally, this indirectly causes microstructure to be implicitly coupled to the experimentally measured oxidation rate.

The primary advantage of the model approach outlined here is the decoupling of kinetics from the microstructure. Using an intrinsic model allows the same kinetics rate to be applied to every

nuclear graphite. This allows the differences in observed reaction rates to truly be described in terms of microstructure. Describing graphite oxidation in terms of microstructure in turn leads to:

1. a more fundamental understanding of the observed oxidation rates within and between grades
2. a more informative route for modeling changes in oxidation rates due to
    a. different graphite grades as well as variation for a single grade intra-billet, inter-billet, and inter-lot
    b. the influence of irradiation damage and creep on microstructure evolution over graphite's service life
    c. small changes in microstructure due to long-term chronic oxidation by coolant impurities
3. a better starting point for predicting oxidation rates of future nuclear graphite grades

# 6. Research Efforts Towards Enhancing a Microstructurally Dependent Oxidation Model

Ultimately, if the nuclear community of scientists and engineers, wish to understand the oxidation of nuclear graphites outside of a narrow range of experimental data, that only pertains to a specific grade, and likely a specific range of sample sizes, Eqs. (19–30), or a very similar system of equations needs to be developed and solved numerically using an intrinsic oxidation model. Several of the advantages of this approach are described in the previous section.

While Eqs. (19-30) may practically be implemented in a relatively short time frame drawing from currently available nuclear graphite literature, further research is needed to "fine-tune" its implimentation. To fully take advantage of the approach outlined in Section 5, the authors strongly believe further research efforts are needed in the areas discussed below.

## 6.1. Kinetics Models

Accurate kinetics models normalized to RSA are needed. Specific to the graphite-oxygen reaction, models similar to the OTM discussed in Section 3.4 are needed. These models should be able to account for a majority of the observed trends in the oxidation literature. While the OTM is overall a good kinetics model, a more accurate approach may be to combine the OTM with a more stochastic approach to account for differences in active sites as well as cooperative interaction between neighboring active sites.

Additional kinetics experimental data over a wide range of experimental temperatures and oxygen concentrations are also needed. Specific experimental ranges of interest include (1) temperatures higher than 1000 K where the effective chemical reaction rate between graphite and oxygen has not been well characterized, and (2) low- and high-concentrations of molecular

oxygen as these two extremes would promote low- and high-surface coverage environments to study the extremes of the adsorption and desorption elementary reactions. Fully graphitized carbon black may be a potential material for such studies as many sources of carbon black are well characterized in literature [105]. Highly oriented pyrolytic graphite may be another useful graphite material, but high-quality, highly oriented pyrolytic graphite can be prohibitively expensive.

Next, in the event of an actual air ingress, the air will most likely not be purely molecular nitrogen and oxygen as used in many experimental studies. The actual air ingressed will contain small amounts of $H_2(g)$, $H_2O(g)$, $CO(g)$ and $CO_2(g)$. As discussed in Section 4.2, these species may influence the local effective rate of oxidation. Astheir roles and relative importance are not extremely well understood for nuclear graphite, further investigation is needed. However, as noted previously, there is some experimental evidence to suggest that $CO(g)$ in small quantities can retard the graphite-oxygen reaction rate [99, 110, 111] and the addition of $H_2(g)$ and $H_2O(g)$ will increase the rate of reaction for Eq. (17).

Other reaction systems entirely may be of interest, including the kinetics of the graphite-nitrogen reaction. In an extreme accident scenario the fuel of an HTGR may be designed to allow maximum temperatures between 1600°C and 1800°C, depending on fuel chemistry and reactor design [112, 113], and ingressed nitrogen may no longer act as an inert gas in terms of its interaction with graphite [114]. At these extreme temperatures, the $N_2(g)$ and $NO(g)$ reaction with graphite may be appreciable.

Finally, a better understanding of the graphite-$H_2O(g)$ reaction may be useful to predict acute effects of moisture and steam ingress into a HTGR under conditions similar to air ingress. Contescu et al. have taken great strides towards understanding the chonic oxidation via moisture with reasonable success [115, 116]. This is accomplished by stochastically fitting a modified Langmuir-Hinshelwood-type reaction model specific to each graphite grade.

### 6.2. Characterization of Microstructural Oxidation Parameters

To determine the observed rate of oxidation for a specific graphite grade, $S_A$, $D_{eff_{iM}}$, and $k_T$ must be characterized. Related to the determination of $S_A$, accurate methods for the estimation of ASA must be found. This is arguably the most important consideration for characterization of $S_A$. In addition to $S_A$, the ratio of ASA to TSA would likely provide some information regarding the mesostructure of the binder-matrix of graphite. A gas adsorption method may provide a reasonable approach to compare the amounts of ASA and TSA between grades, but many complications exist [105]. Furthermore, typical gas adsorption techniques may be difficult to implement as many nuclear graphites have a small specific surface area on the order of a square meter per gram. A differential thermogravimetric method may prove to be the most feasible to collect such information, but it can only determine relative differences rather than absolute amounts. Moreover, such experiments would need to be performed under conditions where $\phi_n \rightarrow$

0, which would limit experiments to small sample sizes (and thus greater inherent variability) and low temperatures.

Along with $S_A$, the effective transport parameters need to be determined if a transport model is to be implemented. $D_{Eff_{iM}}$ can be approximated through carefully designed permeability measurements and extrapolation of the effective diffusion coefficient from experimental flux measurements [82, 83]. Such methods are approximate as most methods provide steady-state measurements and diffusion into "dead end" pores will not be detected. In a reacting system, dead end pores may contribute significantly to the effective diffusion rate. Conversely, transient techniques can be used, but interpretation of an effective diffusion coefficient from transient data is non-trivial.

Provided a mathematical form of the intrinsic reaction kinetics is well established, an effective diffusion coefficient may also be inversely solved for by using observed reaction rate measurements on graphite samples of multiple characteristic lengths [85]. However, care must be taken with such measurements as all other factors must be accurately accounted for to determine the effective diffusion coefficient with a reasonable level of accuracy and precision.

Measurements of $k_T$ have been made on nuclear graphite through experimental measurment of thermal diffusivity via laser flash techniques [117]. As all three effective parameters are expected to evolve over time, measurements at varying levels of conversion, $\alpha$, are desired as well. To understand $k_T$ and its evolution, an understanding of the microstructure of the filler and binder-matrix is needed, along with the dominant Umklapp-type phonon scattering processes limiting energy transport in graphite at the temperatures of interest. An understanding of the rate limiting step for energy transport within a particular graphite will aid in estimation and prediction of $k_T$ as oxidation continually removes additional carbon.

Ultimately to provide a better understanding of measured structural parameters and their evolution with oxidation, a better understanding of the graphite microstructure is needed on all scales. To understand $S_A$ and $D_{Eff_{iM}}$ specifically, a better understanding of the pore structure is needed. Some specific research questions of interest involving the fabrication process are:

1. How does filler particle size affect pore size and morphology?
2. How does the filler-to-binder-matrix ratio as well as additional densification impregnations affect the pore structure and branching of the open pore structure to smaller/finer pores?
3. How do the different porosity ranges (macro, meso, micro, nano, etc.) and their relative distributions affect oxidation?
4. How does the initial composition of the binder-matrix precursor materials as well as additional densification impregnations affect the ratio of ASA to TSA?

### 6.3. Non-equimolar Gas Transport

Finally, large net molar flux rates can significantly affect the rate of oxygen transfer to graphite RSA, and hence the rate of reaction. The change in mass and heat transfer coefficients due to rapid mass transfer across an interface appears to be fairly well understood for laminar flow across horizontal plates and wedges due to a significant body of work in the 1950s and 1960s and a few more recent numerical solutions [87-91, 118]. The authors are unaware of additional work on different geometries or types of flow, but are relatively unfamiliar with developments in this field of research. Regardless, expertise on this subject matter is highly applicable to the oxidation of graphite by molecular oxygen.

## 7. Summary

The end goal of this review article is to enable the development of advanced and robust oxidation models and methodologies for acute air ingress accident scenarios in the extreme environments of current and future HTGR designs. To accomplish this: (1) The limitations and highly conservative nature of classic kinetics models are discussed. (2) The major as well as more subtle features of the graphite-oxygen reaction are thoroughly covered to promote a better understanding of the reaction system. (3) The foundation of an improved, microstructurally informed, oxidation model is highlighted.

As stressed in Section 2, graphite oxidation in an accident scenario is not in-and-of-itself a real concern, rather the issue is the microstructural change inflicted. A graphite's microstructure is inherently tied to its properties and performance and it is ultimately the degraded properties of the graphite that a designer must use to prove the safe performance of a reactor design. While the conservative application of the classic oxidation model has been demonstrated adequate for the safety of historic graphite reactor designs, the more extreme materials environments inherent to more recently developed high temperature gas-cooled reactor designs may require (or at least benefit significantly from) a more detailed understanding of the microstructural damage inflicted. This level of understanding is unavailable through current models.

To accurately predict the effects of oxidation on graphite components (over a broad range of conditions), an oxidation model should consider the chemical kinetics as well as mass transport and the dynamic evolution of porosity. Based upon the discussion of the graphite-$O_2(g)$ reaction mechanism, effects of mass transfer, and pore structure evolution in Sections 3 and 4, a new model is suggested to account for all three considerations properly. The model uses an intrinsic oxidation rate normalized to the reactive surface area, which permits the same rate equation to be used for all nuclear-grade graphites. Consequently, variation in observed oxidation rates between grades can be attributed to microstructural differences in each grade that can subsequently be quantified and used as microstructural inputs into the oxidation model.

While the model presented has significant advantages over classic kinetics models, experimental validation is needed before it can be can be integrated with existing or newly developed safety codes for HTGRs [119-122]. This will require comparing oxidation rates of nuclear grades of graphite measured under several well-controlled conditions as well as rigorous characterization of physical and microstructural properties. Ultimately, successful implementation of such a model, in the United States for example, would lead to modification of graphite code within the American Society of Mechanical Engineers to incorporate this more robust and broadly applicable model.

## 8. Acknowledgements

This work was performed by Battelle Energy Alliance, LLC under the DOE Idaho Operations Contract DE-AC07-05ID14517.

## 9. References

[1] B.P. P.L.C., BP Statistical Review of World Energy 2016, BP Statistical Review of World Energy, British Petroleum P.L.C., London, England, 2016, pp. 1-46.
[2] A.C. Kadak, The Status of the US High-Temperature Gas Reactors, Engineering 2(1) (2016) 119-123.
[3] D. Petti, R. Hill, J. Gehin, H. Gougar, G. Strydom, F. Heidet, J. Kinsey, C. Grandy, A. Qualls, N. Brown, J. Powers, E. Hoffman, D. Croson, Advanced Demonstration and Test Reactor Options Study, Idaho National Laboratory, 2016.
[4] W.E. Windes, G. Strydom, R. Smith, J.J. Kane, Role of Nuclear Grade Graphite in Controlling Oxidation in Modular HTGRs, Idaho National Laboratory, 2014.
[5] R. Moormann, Phenomenology of Graphite Burning in Air Ingress Accidents of HTRs, Science and Technology of Nuclear Installations 2011 (2011) 13.
[4] S.J. Ball, M. Corradini, S.E. Fisher, R. Gauntt, G. Geffraye, J.C. Gehin, Y. Hassan, D.L. Moses, J.-P. Renier, R. Schultz, T. Wei, S. Basu, Accident and Thermal Fluids Analysis PIRTs, Next Generation Nuclear Plant Phenomena Identification and Ranking Tables (PIRTs), Office of Nuclear Regulatory Research, Oak Ridge, Tennessee, 2008.
[5] R.C. Martineau, R.A. Berry, D.A. Knoll, A Preliminary Investigation of Rapid Depressurization Phenomena Following a Sudden DLOFC in a VHTR, 2009, p. Medium: ED.
[6] C.H. Oh, E.S. Kim, H.C. NO, N.Z. Cho, FINAL REPORT on Experimental Validation of Stratified Flow Phenomena, Graphite Oxidation, and Mitigation Strategies of Air Ingress Accidents, 2011, p. Medium: ED.
[7] R.R. Schultz, A.M. Ougouag, D.W. Nigg, H.D. Gougar, R.W. Johnson, W.K. Terry, C.H. Oh, D.W. McEligot, G.W. Johnsen, G.E. McCreery, W.Y. Yoon, J.W. Sterbentz, J.S. Herring, T.A. Taiwo, T.Y.C. Wei, W.D. Pointer, W.S. Yang, M.T. Farmer, H.S. Khalil, M.A. Feltus, Next Generation Nuclear Plant Methods Research and Development Technical Program Plan, PLN-2498, 2008, p. Medium: ED.
[6] S. Ball, M. Richards, S. Shepelev, Sensitivity Studies of Air Ingress Accidents in Modular HTGRS, 3rd International Topical Meeting on High Temperature Reactor Technology, Johannesburg, South Africa, 2006, pp. 1-8.

[7] R. Moore, C. Oh, B. Merrill, D. Petti, Meeting the thermal-hydraulic analysis needs for advanced gas reactor systems, Conference on High Temperature Reactors, Petten, Netherlands, 2002.
[8] O. Levenspiel, Chemical reaction engineering, Wiley, 1999.
[9] O. Levenspiel, The Chemical Reactor Omnibook, OSU Book Stores, 2002.
[10] M. Eto, F.B. Growcock, Effect of oxidizing environment on the strength of H451, PGX and IG-11 graphites, Carbon 21(2) (1983) 135-147.
[11] A.C. Collins, H.G. Masterson, P.P. Jennings, The effect of oxidation on the compressive strength of graphite, Journal of Nuclear Materials 15(2) (1965) 135-136.
[12] M. Pickup, B. McEnaney, R.G. Cooke, Fracture processes in graphite and the effects of oxidation, Carbon 24(5) (1986) 535-543.
[13] J.L. Wood, R.C. Bradt, P.L. Walker, Oxidation effects on toughness and slow crack growth in polycrystalline graphites, Carbon 18(3) (1980) 179-189.
[14] O. Pierre, B.N. Gareth, M. Brian, Influence of oxidation on toughness parameters for two nuclear grade graphites, Journal of Physics D: Applied Physics 38(8) (2005) 1259.
[15] C. I. Contescu, J. P. Strizak, T. R. Guldan, T. D. Burchell, Effect of Air Oxidation on Pore Structure Development and Mechanical Properties of Nuclear Graphite, ORNL External Report ORNL-TM-2010-197, Oak Ridge National Laboratory (ORNL), 2010.
[16] P.L. Walker, F. Rusinko, L.G. Austin, Gas Reactions of Carbon, Advanced in Catalysis, 1958, pp. 133-221.
[17] ASTM Standard D7219-08, Standard Specification for Isotropic and Near-isotropic Nuclear Graphites, ASTM International, West Conshohocken, Pennsylvania, 2014.
[18] L.R. Radovic, Carbon and graphite reactivity, in: K.H.J. Buschow, R.W. Cahn, M.C. Flemings, B. Ilschner, E.J. Kramer, S. Mahajan (Eds.) Encyclopedia of Materials: science and technology, Elesevier, New York, 2001.
[19] N.R. Laine, F.J. Vastola, P.L. Walker, The Importance of Active Surface Area in the Carbon-Oxygen Reaction, The Journal of Physical Chemistry, 67(10) (1963) 2030-2034.
[20] L.R. Radovic, B. Bockrath, On the Chemical Nature of Graphene Edges: Origin of Stability and Potential for Magnetism in Carbon Materials, Journal of the American Chemical Society, 127(16) (2005) 5917-5927.
[21] L.R. Radovic, A. Suarez, F. Vallejos-Burgos, J.O. Sofo, Oxygen migration on the graphene surface. 2. Thermochemistry of basal-plane diffusion (hopping), Carbon, 49(13) (2011) 4226-4238.
[22] A. Montoya, F. Mondragón, T.N. Truong, First-Principles Kinetics of CO Desorption from Oxygen Species on Carbonaceous Surface, The Journal of Physical Chemistry A, 106(16) (2002) 4236-4239.
[23] S.T. Perry, E.M. Hambly, T.H. Fletcher, M.S. Solum, R.J. Pugmire, Solid-state 13C NMR characterization of matched tars and chars from rapid coal devolatilization, Proceedings of the Combustion Institute, 28(2) (2000) 2313-2319.
[24] N. Chen, R.T. Yang, Ab initio molecular orbital calculation on graphite: Selection of molecular system and model chemistry, Carbon, 36(7) (1998) 1061-1070.
[25] A. Montoya, T.-T.T. Truong, F. Mondragón, T.N. Truong, CO Desorption from Oxygen Species on Carbonaceous Surface: 1. Effects of the Local Structure of the Active Site and the Surface Coverage, The Journal of Physical Chemistry A, 105(27) (2001) 6757-6764.
[26] M.H. Back, Comment on “an update on the carbon-oxygen reaction”, Carbon, 29(8) (1991) 1290-1291.

[27] L.R. Radovic, A.F. Silva-Villalobos, A.B. Silva-Tapia, F. Vallejos-Burgos, On the mechanism of nascent site deactivation in graphene, Carbon, 49(11) (2011) 3471-3487.
[28] A.B. Silva-Tapia, X. García-Carmona, L.R. Radovic, Similarities and differences in O2 chemisorption on graphene nanoribbon vs. carbon nanotube, Carbon, 50(3) (2012) 1152-1162.
[29] J.J. Kane, C. Karthik, R. Ubic, W.E. Windes, D.P. Butt, An oxygen transfer model for high purity graphite oxidation, Carbon, 59 (2013) 49-64.
[30] L.R. Radovic, Active Sites in Graphene and the Mechanism of CO2 Formation in Carbon Oxidation, Journal of the American Chemical Society, 131(47) (2009) 17166-17175.
[31] D.R. Olander, R.H. Jones, J.A. Schwarz, W.J. Siekhaus, Reactions of Modulated Molecular Beams with Pyrolytic Graphite. II Oxidation of the Prism Plane, The Journal of Chemical Physics, 57(1) (1972) 421-433.
[32] A. Sánchez, F. Mondragón, Role of the Epoxy Group in the Heterogeneous CO2 Evolution in Carbon Oxidation Reactions, The Journal of Physical Chemistry C, 111(2) (2007) 612-617.
[33] L.R. Radovic, A.B. Silva-Tapia, F. Vallejos-Burgos, Oxygen migration on the graphene surface. 1. Origin of epoxide groups, Carbon, 49(13) (2011) 4218-4225.
[34] J.F. Orrego, F. Zapata, T.N. Truong, F. Mondragón, Heterogeneous CO2 Evolution from Oxidation of Aromatic Carbon-Based Materials, The Journal of Physical Chemistry A, 113(29) (2009) 8415-8420.
[35] C.I. Contescu, T. Guldan, P. Wang, T.D. Burchell, The effect of microstructure on air oxidation resistance of nuclear graphite, Carbon, 50(9) (2012) 3354-3366.
[36] S.G. Chen, R.T. Yang, F. Kapteijn, J.A. Moulijn, A new surface oxygen complex on carbon: toward a unified mechanism for carbon gasification reactions, Industrial & Engineering Chemistry Research, 32(11) (1993) 2835-2840.
[37] J.M. Jones, D.H. Jones, Modelling the competition between annealing and oxidation in the carbon–oxygen reaction, Carbon, 45(3) (2007) 677-680.
[38] O. Senneca, P. Salatino, S. Masi, The influence of char surface oxidation on thermal annealing and loss of combustion reactivity, Proceedings of the Combustion Institute, 30(2) (2005) 2223-2230.
[39] P.L. Walker, Carbon: An old but new material revisited, Carbon, 28(2) (1990) 261-279.
[40] J.M. Thomas, Reactivity of carbon: Some current problems and trends, Carbon, 8(4) (1970) 413-421.
[31] P.L. Walker, R.L. Taylor, J.M. Ranish, An update on the carbon-oxygen reaction, Carbon, 29(3) (1991) 411-421.
[42] N.R. Laine, A mass spectrometric study of the carbon-oxygen reaction—27 years later, Carbon, 29(6) (1991) 729-733.
[43] F.J. Vastola, P.J. Hart, P.L. Walker, A study of carbon-oxygen surface complexes using O18 as a tracer, Carbon, 2(1) (1964) 65-71.
[44] P.J. Hart, Oxygen-18 tracer and low temperature chemisorption studies of the carbon-oxygen reaction, Pennsylvania State University, 1966.
[45] K. Skokova, L.R. Radovic, On the role of carbon-oxygen surface complexes in the carbon/oxygen reaction mechanism, American Chemical Society, 1996.
[46] T. Kyotani, C.A. Leon Y Leon, L.R. Radovic, Simulation of carbon gasification kinetics using an edge recession model, AIChE Journal, 39(7) (1993) 1178-1185.
[47] A.A. Lizzio, H. Jiang, L.R. Radovic, On the kinetics of carbon (Char) gasification: Reconciling models with experiments, Carbon, 28(1) (1990) 7-19.

[48] S.-H. Chi, G.-C. Kim, Comparison of the oxidation rate and degree of graphitization of selected IG and NBG nuclear graphite grades, Journal of Nuclear Materials, 381(1–2) (2008) 9-14.
[49] H.-K. Hinssen, K. Kühn, R. Moormann, B. Schlögl, M. Fechter, M. Mitchell, Oxidation experiments and theoretical examinations on graphite materials relevant for the PBMR, Nuclear Engineering and Design, 238(11) (2008) 3018-3025.
[50] H. Kawakami, Air oxidation behavior of carbon and graphite materials for HTGR, Tanso, 124 (1994) 8.
[51] E.S. Kim, H.C. No, Experimental study on the oxidation of nuclear graphite and development of an oxidation model, Journal of Nuclear Materials, 349(1–2) (2006) 182-194.
[52] E.S. Kim, H.C. No, B.J. Kim, C.H. Oh, Estimation of graphite density and mechanical strength variation of VHTR during air-ingress accident, Nuclear Engineering and Design, 238(4) (2008) 837-847.
[53] J.J. Lee, T.K. Ghosh, S.K. Loyalka, Oxidation rate of nuclear-grade graphite NBG-18 in the kinetic regime for VHTR air ingress accident scenarios, Journal of Nuclear Materials, 438(1–3) (2013) 77-87.
[54] J.J. Lee, T.K. Ghosh, S.K. Loyalka, Oxidation rate of nuclear-grade graphite IG-110 in the kinetic regime for VHTR air ingress accident scenarios, Journal of Nuclear Materials, 446(1–3) (2014) 38-48.
[55] E. Loren Fuller, J.M. Okoh, Kinetics and mechanisms of the reaction of air with nuclear grade graphites: IG-110, Journal of Nuclear Materials, 240(3) (1997) 241-250.
[56] R. Moormann, H.-K. Hinssen, K. Kühn, Oxidation behaviour of an HTR fuel element matrix graphite in oxygen compared to a standard nuclear graphite, Nuclear Engineering and Design, 227(3) (2004) 281-284.
[57] L. Xiaowei, R. Jean-Charles, Y. Suyuan, Effect of temperature on graphite oxidation behavior, Nuclear Engineering and Design, 227(3) (2004) 273-280.
[58] H. Yang, H. Eun, D. Lee, C. Jung, K. Lee, Analysis of combustion kinetics of powdered nuclear graphite by using a nonisothermal thermogravimetric method, Journal of Nuclear Science and Technology, 43 (2006) 4.
[59] C.I. Contescu, S. Azad, D. Miller, M.J. Lance, F.S. Baker, T.D. Burchell, Practical aspects for characterizing air oxidation of graphite, Journal of Nuclear Materials, 381(1–2) (2008) 15-24.
[60] T. Enoki, S. Fujii, K. Takai, Zigzag and armchair edges in graphene, Carbon, 50(9) (2012) 3141-3145.
[61] K. Sendt, B.S. Haynes, Density functional study of the chemisorption of O2 on the zig-zag surface of graphite, Combustion and Flame, 143(4) (2005) 629-643.
[62] G. Dobrik, L. Tapasztó, L.P. Biró, Selective etching of armchair edges in graphite, Carbon, 56 (2013) 332-338.
[63] J.M. Thomas, Chemistry and Physics of Carbon, Philip L. Walker, Jr. ed., Marcel Dekker, New York, 1965.
[64] R.C. Bansal, F.J. Vastola, P.L. Walker, Studies on ultraclean carbon surfaces, Journal of Colloid and Interface Science, 32(2) (1970) 187-194.
[65] R.H. Hurt, B.S. Haynes, On the origin of power-law kinetics in carbon oxidation, Proceedings of the Combustion Institute, 30(2) (2005) 2161-2168.
[66] P.L. Walker, L.G. Austin, J.J. Tietjen, Oxygen chemisorption effects on graphite thermoelectric power, in: P.L. Walker (Ed.), Chemistry and Physics of Carbon, Dekker, New York, 1965, pp. 327-365.

[67] S. Ahmed, M.H. Back, The role of the surface complex in the kinetics of the reaction of oxygen with carbon, Carbon, 23(5) (1985) 513-524.
[68] S.R. Kelemen, H. Freund, O2 oxidation studies of the edge surface of graphite, Carbon, 23(6) (1985) 619-625.
[69] B. Marchon, J. Carrazza, H. Heinemann, G.A. Somorjai, TPD and XPS studies of O2, CO2, and H2O adsorption on clean polycrystalline graphite, Carbon, 26(4) (1988) 507-514.
[70] J. Mira, C.G. Fernández, J.M. Urreaga, Two Examples of Deterministic versus Stochastic Modeling of Chemical Reactions, Journal of Chemical Education, 80(12) (2003) 1488.
[71] B.S. Haynes, T.G. Newbury, Oxyreactivity of carbon surface oxides, Proceedings of the Combustion Institute, 28(2) (2000) 2197-2203.
[72] Z. Du, A.F. Sarofim, J.P. Longwell, Activation energy distribution in temperature-programmed desorption: modeling and application to the soot oxygen system, Energy & Fuels, 4(3) (1990) 296-302.
[73] R.H. Hurt, J.M. Calo, Semi-global intrinsic kinetics for char combustion modeling†, Combustion and Flame, 125(3) (2001) 1138-1149.
[74] M.S. El-Genk, J.-M.P. Tournier, Development and validation of a model for the chemical kinetics of graphite oxidation, Journal of Nuclear Materials, 411(1–3) (2011) 193-207.
[75] M.S. El-Genk, J.-M.P. Tournier, Comparison of oxidation model predictions with gasification data of IG-110, IG-430 and NBG-25 nuclear graphite, Journal of Nuclear Materials, 420(1–3) (2012) 141-158.
[76] M.S. El-Genk, J.-M.P. Tournier, C.I. Contescu, Chemical kinetics parameters and model validation for the gasification of PCEA nuclear graphite, Journal of Nuclear Materials, 444(1–3) (2014) 112-128.
[77] W.P. Eatherly, E.L. Piper, CHAPTER TWO - Manufacture A2 - NIGHTINGALE, R.E, Nuclear Graphite, Academic Press, 2013, pp. 21-51.
[78] F.G. Emmerich, Evolution with heat treatment of crystallinity in carbons, Carbon, 33(12) (1995) 1709-1715.
[79] Fogler, Elements of Chemical Reaction Engineering, 4 ed., Pearson Education International, Upper Saddle River, N.J, 2006.
[80] E.E. Petersen, Chemical reaction analysis [by] Eugene E. Petersen, Prentice-Hall, Englewood Cliffs, NJ, 1965.
[81] E.L. Cussler, Diffusion : mass transfer in fluid systems, Cambridge University Press, Cambridge; New York, 2009.
[82] J. Szekely, J.W. Evans, H.Y. Sohn, Gas-solid reactions, Academic Press, New York, 1976.
[83] C.N. Satterfield, T.K. Sherwood, The role of diffusion in catalysis, Addison-Wesley Pub. Co., Reading, Mass., 1963.
[84] R. Hughes, Deactivation of catalysts, Academic Press, London; Orlando, 1984.
[85] C.N. Satterfield, Mass transfer in heterogeneous catalysis, M.I.T. Press, Cambridge, Mass., 1969.
[82] R. Prober, W.E. Stewart, Transport phenomena in wedge flows: Pertubration solutions for small mass transfer rates ERRATA, International Journal of Heat and Mass Transfer, 6(9) (1963) 872.
[87] R. Prober, W.E. Stewart, Transport phenomena in wedge flows: Perturbation solutions for small mass transfer rates, International Journal of Heat and Mass Transfer, 6(3) (1963) 221-229.
[88] W.E. Stewart, R. Prober, Heat transfer and diffusion in wedge flows with rapid mass transfer, International Journal of Heat and Mass Transfer, 5(12) (1962) 1149-1163.

[89] H.L. Evans, Mass transfer through laminar boundary layers—6. Methods of evaluating the wall gradient (b'0/B) for similar solutions; some new values for zero main-stream pressure gradient, International Journal of Heat and Mass Transfer, 3(4) (1961) 321-339.
[90] O. Aydın, A. Kaya, Laminar boundary layer flow over a horizontal permeable flat plate, Applied Mathematics and Computation, 161(1) (2005) 229-240.
[91] R.B. Bird, W.E. Stewart, E.N. Lightfoot, Interphase Transport In Nonisothermal Mixtures, Transport phenomena, J. Wiley, New York, 2007.
[92] J.R. Arthur, Reactions between carbon and oxygen, Transactions of the Faraday Society, 47(0) (1951) 164-178.
[93] V.M. Rossberg, Experimentelle Ergebnisse uber die Pimarreaktionen bei der Kohlenstoffverbrennung, Z. Elektrochem, 60 (1956) 952-956.
[94] M.S. El-Genk, J.-M.P. Tournier, Sherwood number correlation for nuclear graphite gasification at high temperature, Progress in Nuclear Energy, 62 (2013) 26-36.
[95] P. Glarborg, D. Kubel, P.G. Kristensen, J. Hansen, K. Dam-Johansen, Interactions of CO, NOx and H2O Under Post-Flame Conditions, Combustion Science and Technology, 110-111(1) (1995) 461-485.
[96] M.A. Mueller, T.J. Kim, R.A. Yetter, F.L. Dryer, Flow reactor studies and kinetic modeling of the H2/O2 reaction, International Journal of Chemical Kinetics 31(2), (1999) 113-125.
[97] R.A. Yetter, F.L. Dryer, H. Rabitz, A Comprehensive Reaction Mechanism For Carbon Monoxide/Hydrogen/Oxygen Kinetics, Combustion Science and Technology, 79(1-3) (1991) 97-128.
[98] R.J. Kee, M.E. Coltrin, P. Glarborg, High-Temperature Chemistry, Chemical Reacting Flow Theory and Practice, John Wiley and Sons, Inc., Hoboken, New Jersey, 2003, pp. 584-586.
[99] J.M. Ranish, P.L. Walker, Effect of small concentrations of CO on rate of gasification of spectroscopic graphite in $O_2$, Carbon, 24(2) (1986) 109-114.
[100] J. Rouquerol, D. Avnir, C.W. Fairbridge, D.H. Everett, J.H. Haynes, N. Pernicone, J.D.F. Ramsay, K.S.W. Sing, K.K. Unger, Recommendations for the characteriation of porous solids (Technical Report), Pure and Applied Chemistry, 66(8) (1994) 19.
[101] L.L. Snead, C.I. Contescu, T.S. Byun, W. Porter, Thermophysical property and pore structure evolution in stressed and non-stressed neutron irradiated IG-110 nuclear graphite, Journal of Nuclear Materials, 476 (2016) 102-109.
[102] Z. Mileeva, D.K. Ross, S.M. King, A study of the porosity of nuclear graphite using small-angle neutron scattering, Carbon, 64 (2013) 20-26.
[103] C.J. Gommes, A.-J. Bons, S. Blacher, J.H. Dunsmuir, A.H. Tsou, Practical methods for measuring the tortuosity of porous materials from binary or gray-tone tomographic reconstructions, AIChE Journal, 55(8) (2009) 2000-2012.
[104] E.E. Petersen, Diffusion in a pore of varying cross section, AIChE Journal 4(3) (1958) 343-345.
[105] F. Rouquerol, J. Rouquerol, K.S.W. Sing, Adsorption by powders and porous solids : principles, methodology, and applications, (1999) 237-285.
[106] M. Richards, REACT_COMPACT: A computer code for modeling graphite corrosion and fuel hyrdolysis, 2016 International Topical Meeting on High Temperature Reactor Technology (HTR2016), Las Vegas, Nevada, USA, 2016, pp.1-10.
[107] X. Wei, S. Lei, Z. Yanhua, Transient analysis of nuclear graphite oxidation for high temperature gas cooled reactor, Nuclear Engineering and Design, 306 (2016) 138-144.

[108] A.N. Odeichuk, A.I. Komir, Simulation of Graphite Oxidation in Oxygen at 400-800°C, Physics of Particles and Nuclei Letters, 12(2) (2015) 255-361.
[109] R.P. Wichner, T.D. Burchell, C.I. Contescu, Penetration depth and transient oxidation of graphite by oxygen and water vapor, Journal of Nuclear Materials, 393 (2009) 518-521.
[110] J.M. Ranish, Kinetics of the carbon oxygen reaction, Pennsylvania State University, University Park, Pennsylvania, 1984.
[111] J.F. Espinal, A. Montoya, F. Mondragón, T.N. Truong, A DFT Study of Interaction of Carbon Monoxide with Carbonaceous Materials, The Journal of Physical Chemistry B, 108(3) (2004) 1003-1008.
[112] R.N. Morris, C.A. Baldwin, P.A. Demkowicz, J.D. Hunn, E.L. Reber, Performance of AGR-1 high-temperature reactor fuel during post-irradiation heating tests, Nuclear Engineering and Design, 306 (2016) 24-35.
[113] Y. Zheng, L. Shi, Y. Dong, Thermohydraulic transient studies of the Chinese 200 MWe HTR-PM for loss of forced cooling accidents, Annals of Nuclear Energy, 36(6) (2009) 742-751.
[114] A.M. Oyarzún, L.R. Radovic, T. Kyotani, An update on the mechanism of the graphene–NO reaction, Carbon, 86 (2015) 58-68.
[115] C.I. Contescu, R.W. Mee, P. Wang, A.V. Romanova, T.D. Burchell, Oxidation of PCEA nuclear graphite by low water concentrations in helium, Journal of Nuclear Materials, 453(1–3) (2014) 225-232.
[116] C.I. Contescu, R.W. Mee, Status of Chronic Oxiation Studies of Graphite, Oak Ridge National Laboratory, 2016.
[117] W. David Swank, W.E. Windes, Specimen size effects in the determination of nuclear grade graphite thermal diffusivity, in: N. Tzelepi, M. Carroll (Eds.) ASTM International, 2014, p. 13.
[118] R. Prober, W.E. Stewart, Int. j. heat mass transfer, International Journal of Heat and Mass Transfer 6(9) (1963) 872.
[119] R. Moore, C. Oh, B. Merrill, D. Petti, Studies on air ingress for pebble bed reactors, Proceeding of the high temperture reactors conference, Petten, Netherland, 2002.
[120] C.H. Oh, C. Davis, L. Siefken, R. Moore, H.C. No, J. Kim, G.C. Park, J.C. Lee, W.R. Martin, Development of safety analysis codes and experimental validation for a very high temperature gas-cooled reactor Final report, Idaho National Laboratory (INL), 2006, p. Medium: ED.
[121] S.J. Ball, MORECA: A computer code for simulating modular high-temperature gas-cooled reactor core heatup accidents, ; Nuclear Regulatory Commission, Washington, DC (United States). Div. of Regulatory Applications; Oak Ridge National Lab., TN (United States), 1991, p. Medium: ED; Size: Pages: (63 p).
[122] S.J. Ball, D.J. Nypaver, GRSAC users manual, Oak Ridge National Laboratory, Instrumentation and Controls Division, Oak Ridge Tennesse, 1999.